Title

Carbon partitioning and metabolic control by the TPT3 triose phosphate translocator of *Chlamydomonas reinhardtii*

Weichao Huang[1]†*, Anagha Krishnan[2]†, Anastasija Plett[3], Michelle Meagher[4], Nicole Linka[3], Yongsheng Wang[5], Bijie Ren[1], Justin Findinier[1], Petra Redekop[1], Neda Fakhimi[1], Rick G. Kim[1], Devin A. Karns[2], Nanette Boyle[4], Matthew C. Posewitz[2], Arthur R. Grossman[1]*

[1]Department of Plant Biology, Carnegie Institution for Science, Stanford, CA 94305, USA

[2]Department of Chemistry, Colorado School of Mines, Golden, CO 80401, USA

[3]Institute of Plant Biochemistry, Heinrich-Heine University Düsseldorf, 40225 Düsseldorf, Germany

[4]Department of Chemical and Biological Engineering, Colorado School of Mines, Golden, CO 80401, USA

[5]School of Life Sciences, Tsinghua University, 100084 Beijing, China

†Authors contributed equally.

*Corresponding Author: Weichao Huang; Address: The Carnegie Institution for Science, 260 Panama St. Bldg. 100; Stanford, CA 94305; email: whuang@carnegiescience.edu

*Corresponding Author: Arthur R. Grossman; Address: The Carnegie Institution for Science, 260 Panama St. Bldg. 100; Stanford, CA 94305; email: agrossman@carnegiescience.edu

Running title

Triose phosphate/phosphate translocator: a dominant factor in regulating compartmentalized metabolism and photosynthetic activity in Chlamydomonas

Abstract

Modulation of the rates of export of photoassimilates from the chloroplast is essential for maintaining optimum photosynthetic rates. Additionally, the export of carbon metabolites from the chloroplast can serve in the transduction of chloroplast signals to the nucleus in response to environmental stresses. In this study we characterized a major chloroplast translocator of fixed carbon, the triose phosphate/phosphate translocator 3 (CreTPT3), of the green alga *Chlamydomonas reinhardtii*. This translocator is expressed at high levels, was shown to be on the chloroplast envelope membrane and preferentially exchanges DHAP and 3-PGA for Pi based on an in vitro yeast liposome uptake assay. Null mutants for CreTPT3, generated by CRISPR-Cas9, exhibited a pleiotropic phenotype that impacted the growth, the rate of photosynthetic electron transport, metabolite profiles, carbon partitioning, and organelle-specific accumulation of H_2O_2. The severe phenotype of the *tpt3* mutant demonstrates that this transporter is a dominant conduit on the chloroplast envelope for the transport of photosynthetically fixed carbon. In addition, CreTPT3 can serve as a safety valve that moves excess reductant out of the chloroplast which helps stabilize the redox state of the plastid. Finally, we demonstrated that CreTPT3 is essential for preventing the cells from experiencing oxidative stress by sustaining a high rate of photosynthetic electron transport as the cells acclimate to high light. Our studies reveal important features about the localization and activity of CreTPT3, its importance in controlling metabolite partitioning, and suggest differences in the export of photoassimilates from the chloroplasts of Chlamydomonas and vascular plants.

Introduction

Photosynthetic organisms can absorb excess, potentially damaging levels of light energy during mid-day (when photosynthetic electron transport becomes saturated) and can suffer from extreme damage, especially when experiencing rapid fluctuations in light intensities or are subjected to nutrient limiting conditions and other environmental stresses that impair the productive utilization of excitation energy (Chaux et al., 2017; Saroussi et al., 2017). To cope with excess excitation energy, plants and algae have evolved mechanisms to dissipate this energy through nonphotochemical quenching (NPQ). The excess reductant and energy can also be eliminated by photochemical quenching. While the dominant form of photochemical quenching often involves the use of the electrons/reductant to fix inorganic carbon (Ci), which is used for growth or stored in the form of starch and lipids (Ge et al., 2014; Huang et al., 2018; Krishnan et al., 2015), redox equivalents can also be trafficked to other outlets where they are not used for anabolic processes. The main alternative photochemical electron outlets involve the reduction of O_2 to H_2O in H_2O-to-H_2O cycles that include a (*i*) Mehler-type reaction that is noncatalytic and functions on the acceptor side of PSI, (*ii*) flavodiiron protein reactions (Jokel et al., 2018) (FLVs, NADPH:flavin oxidoreductase) that catalytically reduces O_2 on the acceptor side of PSI without generating reactive oxygen species (ROS), (*iii*) the plastid terminal oxidase (Houille-Vernes et al., 2011) (PTOX, plastoquinol: oxygen oxidoreductase) reaction that can use electrons from the PQ pool to reduce O_2, and (*iv*) the movement of redox equivalents from the chloroplast to the mitochondrion where they can be used to reduce O_2 through various electron transport activities.

Mechanisms also exist in which fixed carbon and reducing equivalents can be shuttled between the chloroplast and cytoplasm. Studies with *Arabidopsis thaliana* revealed that the malate shuttle, which involves multiple malate dehydrogenases (MDH) and malate/OAA translocators (OMT), functions in the export of reductant from the chloroplast and enables plant cells to manage redox conditions in the chloroplast (Zhao et al., 2018, 2020). In addition to the malate shuttle, the triose phosphate (triose-P)/phosphate (Pi) translocator (TPT) has been proposed to be involved in moving fixed carbon out of the chloroplast, but can also act as a potential safety valve for eliminating excess reducing power from the chloroplast (Fliege et al., 1978; Flügge et al., 1989; Johnson and Alric, 2013; Lee et al., 2017a; Raghavendra and Padmasree, 2003; Stocking and Larson, 1969). The synthesis of triose-Ps during photosynthetic CO_2 fixation by the Calvin-Benson-Bassham Cycle (CBBC) is supported by the reducing power/energy (NADPH, ATP)

80 derived from photosynthetic electron transport. The TPTs reside on the inner chloroplast envelope
81 membrane and can transport triose-Ps (glyceraldehyde 3-phosphate (GAP), dihydroxyacetone
82 phosphate (DHAP)) and the three carbon acid 3-phosphoglycerate (3-PGA) in a counter exchange
83 for cytosolic Pi (Fliege et al., 1978; Flügge et al., 1989; Lee et al., 2017b).

84 During the last decades, physiological functions of the TPTs have been examined. Various plants
85 do not exhibit a strong phenotype if the chloroplast TPT is either eliminated or its level is reduced
86 (Häusler et al., 1998; Riesmeier et al., 1993; Schneider et al., 2002; Walters et al., 2004). A
87 reduction in TPT activity can be compensated for by diverting assimilated carbon into a transitory
88 starch pool that is subjected to accelerated turnover in the light and/or dark (Häusler et al., 1998;
89 Riesmeier et al., 1993; Walters et al., 2004), leading to accumulation of starch degradation
90 products that can be exported from the chloroplast and used in other cellular compartments.
91 Interestingly, a deficiency of the TPT in rice, which uses sucrose stored in leaves as its major
92 transitory form of fixed carbon rather than starch, led to severe phenotypic consequences; the
93 plants exhibited reduced photosynthetic rates and decreased levels of both starch and soluble
94 sugars relative to WT plants (Lee et al., 2014). In addition to the TPTs, plant chloroplasts possess
95 a maltose transporter (MEX1) and glucose translocator (GlcT), both of which are important for the
96 export of starch degradation products (Cho et al., 2011; Niittylä et al., 2004). Growth of
97 *Arabidopsis thaliana* mutants lacking the GlcT (*pglct-1* and *pglct-2*) was not significantly
98 impacted. In contrast, an Arabidopsis mutant defective for the maltose transporter (*mex1*)
99 displayed severe growth retardation (Niittylä et al., 2004). To further investigate the functions of
100 these sugar transporters in plant growth and development, double mutants of Arabidopsis lacking
101 MEX1 and either TPT or GlcT (Cho et al., 2011) were generated. The *pglct-1*/*mex1* and *tpt-2*/*mex1*
102 double mutants displayed strong growth inhibition, even relative to the *mex1* single mutant, with
103 the *pglct-1*/*mex1* strain exhibiting the most severe growth phenotype. In addition, *pglct-1*/*mex1*
104 displayed severely reduced photosynthetic activities and extreme aberrations in chloroplast
105 morphology. These studies demonstrated that in plants, the starch-mediated pathway for the export
106 of photoassimilate via GlcT and MEX1 is essential for Arabidopsis growth and development (Cho
107 et al., 2011).

108 Microalgae have high photosynthetic conversion efficiencies, can thrive in fresh to hypersaline
109 waters and are among the most metabolically versatile organisms known. They have also attracted
110 considerable interest worldwide because of their ability to synthesis large quantities of lipids (e.g.

111 for biofuels and food products), starch, pigments and other bioproduction, and can serve in the
112 remediation of waste water (Bhatt et al., 2022; Khan et al., 2018). Furthermore, the transporters
113 used for moving photoassimilate between the chloroplast and other cellular compartments and the
114 mechanisms and regulation of these transporters in microalgae have not been extensively explored.
115 Understanding the activities that comprise metabolite transport into and out of chloroplasts is
116 linked to an understanding of the metabolisms associated with the chloroplast, which can differ in
117 plants and algae; this is exemplified by the compartmentalization of the glycolytic and oxidative
118 pentose-phosphate pathways (OPPP). Plants appear to have duplicated the entire glycolytic and
119 OPPP pathways, with these pathways localized to both the chloroplast and cytosol (Plaxton, 1996).
120 In green microalgae such as the unicellular green alga *Chlamydomonas reinhardtii*
121 (Chlamydomonas throughout), the glycolytic pathway is not duplicated but is highly
122 compartmentalized, with the "upper half" of glycolysis (from glucose to GAP) exclusively in the
123 chloroplast and the "lower half" (from 3-PGA to pyruvate) exclusively in the cytosol (Klein, 1986).
124 Such metabolic differences suggest that metabolite exchange between the chloroplast and cytosol
125 is likely to differ between land plants and Chlamydomonas. Developing a more informed
126 understanding of central metabolism in microalgae can enable additional work on the
127 establishment, regulation and evolution of metabolic networks in algae and the ways in which
128 algae can be tailored for production purposes and for sustained growth under specific
129 environmental conditions.

130 One group of highly expressed translocators associated with movement of triose-P between the
131 chloroplast and cytosol are in the TPT family, a subgroup in the drug/metabolite transporter (DMT)
132 superfamily. There are still relatively few studies that demonstrate the functionalities of TPT
133 translocators in single-celled photosynthetic organisms (red algae, green algae, cryptophyte) based
134 on in vitro activities of these proteins in liposome transport assays (Haferkamp et al., 2006; Linka
135 et al., 2008; Moog et al., 2020). Active transport of triose phosphates has been noted multiple times
136 in Chlamydomonas (Boschetti and Schmid, 1998; Klöck and Kreuzberg, 1991), although, the
137 physiological fuctions associated with the various TPTs encoded on the genome of this alga have
138 not been characterized.

139 In this study, we used Chlamydomonas, the well-established model green algal system that has
140 been extensively used to analyze various physiological processes and, more specifically, to dissect
141 the function of its highly expressed TPT3 translocator. Chlamydomonas is predicted to contain

142 more than 30 TPT homologs; the informatic analyses of these proteins are still not refined enough
143 to be certain of their substrate specificities and, in many cases, the transported metabolites are
144 likely not triose-Ps. Here we present work that approaches the questions: *i*) what are the roles of
145 chloroplast TPTs in partitioning fixed carbon and sustaining central carbon metabolism? *ii*) how
146 do changes in the activities of these transporters, and in particular TPT3, impact photosynthetic
147 electron transport (PET)? *iii*) what is the relationship between the transport of triose-P from
148 chloroplasts and the production of ROS? Our analyses have been focused on Chlamydomonas
149 TPT3 (CreTPT3) which, among the four predicted chloroplast associated TPT-like transporters, is
150 the one most similar to plant chloroplast TPTs, and is highly expressed in the light. Through a
151 series of in vitro and physiological analyses, we demonstrated that CreTPT3 is a major conduit on
152 the chloroplast envelope for the trafficking of fixed carbon, sustaining central carbon metabolism,
153 dissipating excess energy, enabling high rates of photosynthetic electron transport, preventing
154 intracellular hydrogen peroxide (H_2O_2) accumulation, and balancing redox conditions at the
155 subcellular level.

156 **Results**

157 **Features of the triose-P/Pi translocator (DMT/TPT) family**

158 Candidate genes encoding triose-P/Pi transporters (TPT) of Chlamydomonas were identified by
159 blasting the Arabidopsis TPT protein (AT5G46110.1) against proteins encoded on the
160 Chlamydomonas genome. The TPT family is the largest within the DMT superfamily in
161 eukaryotes and includes triose-P and sugar-phosphate transporters associated with chloroplasts;
162 many the family members are still not functionally characterized (Jack et al., 2001; Knappe et al.,
163 2003; Weber et al., 2006). We have identified 32 genes encoding potential TPTs in the version
164 v6.1 genome of Chlamydomonas, with four members, CreTPT10 (CreTPT1 in v5.6 genome),
165 CrePPT2 (CreTPT2 in v5.6 genome), CreTPT3 and CGL51 (CreTPT25 in v5.6 genome), predicted
166 to have a chloroplast-localized transit peptide (**Supplementary Table 3**).

167 Land plants harbor four classes of phosphate translocators on the inner plastid envelope that import
168 and/or export sugars, including glucose 6-phosphate (GPT, transports glucose 6-phosphate),
169 xylulose phosphate (XPT, transports xylulose 6-phosphate), phosphoenolpyruvate (PPT), and
170 triose-P (various TPTs) (Eicks et al., 2002; Fischer et al., 1997; Flügge et al., 1989; Kammerer et
171 al., 1998; Lee et al., 2017a). To explore the potential substrate specificities of the four putative

172 chloroplast-localized, Chlamydomonas TPT family transporters, their amino acid sequences were
173 aligned with the plastidial phosphate transporters (PT) from Arabidopsis (AtPTs) (**Supplementary**
174 **Fig. 2**). The ability of these transporters to use triose-P/DHAP or 3-PGA as substrate is dependent
175 on five highly conserved residues (H184, K203, Y338, K359, and R360 in AtTPT1) (Lee et al.,
176 2017a; Moog et al., 2020). Of the four putative chloroplast-targeted TPT family members in
177 Chlamydomonas, only CreTPT3 and CGL51 contain all five of these residues (H170, K189, Y322,
178 K345, and R346 in CreTPT3) (**Supplementary Fig. 2**). In AtTPT1, residue F262 (F248 in
179 Chlamydomonas in the analogous protein CreTPT3) is thought to inhibit phosphoenolpyruvate
180 (PEP) access to the binding site; this residue is replaced by N in AtPPT1 (PPT) (Lee et al., 2017a;
181 Moog et al., 2020). CGL51 has M at position F248, indicating that unlike the other
182 Chlamydomonas putative chloroplast sugar phosphate transporters, CGL51 might have greater
183 preference for PEP or other substrates. These findings suggest that of the four chloroplast TPT
184 family members, CreTPT3 most likely functions in specifically shuttling triose-P or 3-PGA across
185 the chloroplast envelope.

186 **TPT3 transport properties**

187 To help establish the physiological (in vivo) function of CreTPT3, its deduced subcellular
188 localization was experimentally determined. The CreTPT3 coding sequence with its putative
189 targeting sequence was fused with VENUS (CreTPT3-VENUS) and expressed under the control
190 of its own promoter in a Chlamydomonas mutant null for CreTPT3 (*t3ko2*, see below). As shown
191 in **Fig. 1A**, CreTPT3-VENUS localized to the chloroplast envelope.

192 To evaluate the substrate specificity of CreTPT3, it was expressed in *Saccharomyces cerevisiae*
193 (yeast) and the resulting recombinant protein was biochemically analyzed using a liposome uptake
194 assay. The Cre*TPT3* gene was codon-optimized, expressed in yeast (**Fig. 1B**), and total cell
195 membranes were isolated and reconstituted into liposomes (Linka et al., 2008; Loddenkötter et al.,
196 1993). Chloroplast phosphate transporters in vascular plants can catalyze a Pi/Pi homo-exchange
197 in vitro. The reconstituted CreTPT3 in liposomes was able to catalyze the signature Pi homo-
198 exchange, whereas in the absence of a counter-exchange substrate, little Pi uptake was detected
199 (**Fig. 1C**). In contrast, very low Pi uptake rates were observed for liposomes reconstituted with
200 membranes from yeast cells lacking CreTPT3 (**Supplementary Fig. 3**), indicating that the
201 detected Pi import activity was the result of CreTPT3 expression in yeast.

202 To assess the substrate specificity, the initial rates of Pi uptake into liposomes preloaded with
203 saturating concentrations (30 mM) of various potential counter-exchange substrates were
204 determined. As **Fig. 1D** shows, CreTPT3 exhibited the highest activity when DHAP was used as
205 substrate. The relative initial velocity for Pi uptake in exchange for DHAP was slightly higher than
206 that of 3-PGA (3-PGA exhibited a 75% exchange rate relative to that of Pi/DHAP) while the Pi
207 uptake into liposomes preloaded with PEP was much less efficient (about 16% relative to the
208 Pi/DHAP exchange rate) (**Fig. 1D**). Pi import was negligible when CreTPT3 liposomes were
209 preloaded with Glc-6-P, Glc-1-P, Fru-6-P, and Gal-1-P (**Fig. 1D**).

210 Characterizations of the K_M and K_i of CreTPT3 were performed to determine the affinity of the
211 transporter for the various substrates. CreTPT3 has an apparent Michaelis-Menten constant (K_M)
212 value of 1.1 +/- 0.2 mM for Pi (**Fig. 1E**), which is comparable to the value obtained for the vascular
213 plant TPT ortholog (Flügge et al., 1989). DHAP and 3-PGA competitively inhibited Pi uptake with
214 an inhibition constant (Ki) of 0.57 +/- 0.01 mM and 0.79 +/- 0.12 mM, respectively (**Fig. 1E**),
215 suggesting that CreTPT3 has a higher affinity for DHAP and 3-PGA than for Pi. In the case of
216 PEP, no inhibition of the Pi/Pi homo-exchange was observed, even at the non-physiologically high
217 concentration of 5 mM. Overall, the results of these in vitro assays indicate that CreTPT3 has a
218 typical plant-TPT substrate spectrum (Flügge et al., 1989). It can transport Pi, triose-P (DHAP)
219 and 3-PGA in a counter-exchange mode, however PEP might not be a physiologically relevant
220 substrate for CreTPT3, as was shown for apoplast TPT homologues in other organisms (Lim et al.,
221 2010; Moog et al., 2020).

222 **Isolation of *tpt3* null mutants and their impact on cell growth**

223 To explore the role of CreTPT3 in trafficking carbon and potentially reductant across the
224 chloroplast envelope in vivo, CRISPR knockouts of Cre*TPT3* were generated. We used the
225 CRISPR-Cas9 editing system to disrupt the Cre*TPT3* gene in exons 1 and 7 while at the same time
226 integrating the hygromycin marker gene (*AphVII*) into the edited site (**Fig. 2A**). Multiple
227 independent knockouts of Cre*TPT3* were obtained, including *t3ko1*, with the marker gene inserted
228 into exon 1, and *t3ko2* and *t3ko3*, with the marker gene inserted into exon 7; no CreTPT3 protein
229 was detected in any of the edited strains (**Fig. 2B, Supplementary Fig. 4**).

230 To elucidate the physiological roles of CreTPT3, we first examined growth of the parental WT
231 strain and the knockout mutants under either low light (LL, 30 µmol photons m^{-2} s^{-1}) or moderate

232 light (ML, 250-300 μmol photons m^{-2} s^{-1}). In contrast to WT cells, growth of all three of the
233 Cre*TPT3* knockouts (*t3ko1*, *t3ko2*, *t3ko3*) was significantly reduced in LL on either
234 photoautotrophic (TP) or heterotrophic (TAP) solid agar medium (**Fig. 2C**), while the growth of
235 the mutant in ML was completely blocked on both TP and TAP (**Fig. 2C**). Growth curves were
236 also determined for WT and mutant cells in liquid medium (TP) in both LL and ML (**Fig. 2D**); the
237 results were in accord with those observed for the solid medium growth assays. Additionally, *tpt3*
238 mutant cells in both LL and ML exhibited an increased cell diameter and formed clusters of cells
239 that appear to be less able to separate following cell division (**Supplementary Fig. 5A**, **B**). To
240 further confirm that the growth phenotypes are a consequence of the *tpt3* knockout, we introduced
241 a wild-type copy of Cre*TPT3* fused to VENUS into the mutant strains (**Fig. 2B**). As shown in **Fig.**
242 **2C-F**, ectopic expression of the wild-type Cre*TPT3* in the *t3ko2* mutant (*C_T3KO2*) rescued the
243 reduced growth phenotype of the mutant under all light conditions tested in this study (LL/ML/HL).

244 We also analyzed the chlorophyll content of photoautotrophically grown cells after transferring
245 them from LL to ML (**Supplementary Fig. 1**) and found that *t3ko2* had reduced chlorophyll
246 content relative to WT cells after 24 h in ML (**Fig. 2E-F** and **Supplementary Fig. 6**). Cell numbers
247 and total chlorophyll were quantified following the LL to ML transition. The chlorophyll levels
248 per cell declined in all strains at 24 and 48 h following transfer to ML; however, it was lower by
249 more than half in *t3ko2* (0.34 μg/10^6 cells) relative to either WT cells or the *C_T3KO2* rescued
250 strain (both ~0.72 μg/10^6 cells) after 24 h of ML (**Supplementary Fig. 6**), with some additional
251 increase for WT and *C_T3KO2* after 48 h of ML (which might reflect some shading caused by an
252 increase in the cell density). Finally, when mutant cells were transferred to HL for 24 h they
253 became highly bleached (**Fig. 2E**).

254 Taken together, these results indicate that the activity of the CreTPT3 transporter is essential for
255 growth over a range of light intensities (LL/ML/HL).

256 **The *tpt3* mutant exhibits hyper-accumulation of 'storage' carbon**

257 To explore the impact of the loss of CreTPT3 activity on carbon partitioning, we quantified carbon
258 storage (starch and lipids) following a transition of WT and the *t3ko2* mutant from LL to ML.
259 Lugol staining showed extensive starch accumulation in the *t3ko2* cells after a 48-h exposure to
260 ML, whereas WT cells were barely stained (**Fig. 3B**). Furthermore, as shown in **Fig. 3A**, there is
261 a ~55-fold difference in the level starch that accumulated in *t3ko2* relative to WT cells (13.29

262 compared to 0.24 µg starch/µg chlorophyll, respectively) after 24 h of illumination in ML. The
263 mutant also accumulated ~24-fold more lipid than WT and *C_T3KO2* cells (on a chlorophyll basis),
264 as monitored by Nile Red fluorescence, over the same time period (WT and *t3ko2*: 1038 and 41
265 Nile Red fluorescence/chlorophyll, respectively) (**Fig. 3C**, **D**). Since the chlorophyll in the mutant
266 was approximately 50% relative to that of WT cells after 24 h in ML, the accumulated starch and
267 lipid on a per cell basis would be ~25-fold more starch and ~12-fold more lipid in the mutant
268 relative to the WT strain. Furthermore, mutant cells are much bigger and tend to show more
269 aggregation than WT cells (**Supplementary Fig. 5A**, **B**), which may reflect the large increase of
270 storage carbon that they accumulate. These results suggest that the inability to transport triose-P
271 between the chloroplast and the cytosol through CreTPT3 resulted in a repartitioning of
272 photosynthetic assimilates (carbon, reductant, and ATP) toward the synthesis of both starch and
273 neutral lipid.

274 **Cre*TPT3* deletion leads to accumulation of CBBC/glycolytic/gluconeogenic intermediates**

275 To understand the metabolic consequences of the loss of CreTPT3 on growth under LL and ML,
276 comparative metabolite analyses of WT and the *t3ko2* mutant were performed on cells grown at
277 LL and after shifting them to ML for both 45 min and 6 h. Pool sizes of various central carbon
278 metabolites, particularly those of the CBBC/glycolysis/gluconeogenesis pathways and
279 intermediates of the TCA/glyoxylate cycle (**Fig. 3F**), were quantified. Data was normalized to both
280 chlorophyll content (**Fig. 3E**) and cell number (**Supplementary Fig. 7B**). The fold-change in the
281 quantity of each metabolite in the mutant relative to WT under LL or at 45 min and 6 h after the
282 switch to ML is given in **Fig. 3G** and **Supplementary Fig. 7C**.

283 Under LL (**Fig. 3E**, time 0 h) and following transfer to ML, the *t3ko2* mutant maintained a
284 significantly larger pool (2 to 6-fold) of glycolytic/gluconeogenic intermediates [DHAP, 3-PGA
285 and FBP (all three shared with CBBC), G6P, PEP], and of some metabolites of the CBBC pathway
286 (E4P, RU5P/X5P, R5P) compared to WT cells, suggesting that the loss of CreTPT3 results in a
287 back-up of these metabolites within the cell; our hypothesis is that they are accumulating inside
288 the chloroplast due to the reduced ability to export carbon in the *t3ko2* mutant. This is supported
289 by the finding of marked accumulation of starch and TAG in the mutant strain (**Fig. 3A-D**). While
290 the pool sizes of fumarate and malate (metabolites of the TCA/glyoxylate cycle) were similar in
291 both strains under LL, following the transition of the cells to ML, WT cells exhibited a significant

292 increase in the pool sizes of those metabolites while the mutant maintained a lower level, indicating
293 that the loss of CreTPT3 either directly (by supplying precursors) or indirectly (metabolic rewiring)
294 impacts their levels.

295 Thus, a primary function of CreTPT3 appears to be the export of photosynthetically-synthesized
296 reduced carbon, which would drive metabolic processes in the cytoplasm and other cellular
297 compartments, while importing Pi into the chloroplast to sustain ATP synthesis.

298 **The *tpt3* mutant has reduced photosynthetic activity when grown in ML**

299 To understand the impact of the loss of CreTPT3 activity on PET, we quantified photosynthetic
300 activities following a transition from LL to ML (**Supplementary Fig. 1)**. Photosynthetic O_2
301 evolution rates (OERs) were measured for WT, *t3ko2* and *C_T3KO2* over a range of light
302 intensities. LL acclimated WT, *t3ko2*, and *C_T3KO2* showed comparable OER at intensities below
303 200 μmol photons m^{-2} s^{-1} while at saturating light intensities of ⩾600 μmol photons m^{-2} s^{-1}, the
304 OER of *t3ko2* was diminished slightly relative to the WT and the complemented strain (**Fig. 4A**).
305 Upon acclimation of the cells to ML for 24 h, the *t3ko2* mutant consistently displayed lower OERs
306 than WT or *C_T3KO2* under all actinic light intensities used (**Fig. 4A**). Additionally, the Fv/Fm
307 in the mutant grown in LL was similar to that of WT and *C_T3KO2* (**Fig. 4B**). In contrast, after
308 exposure of the mutant cells to ML for 6 h, the Fv/Fm declined to about 50% of the WT and
309 *C_T3KO2* values; the decline in the mutant continued over a period of 24 h in ML, with a 3-fold
310 decrease in Fv/Fm for *t3ko2* compared to that of WT (**Fig. 4B**). These results indicate that there is
311 damage of PSII reaction centers following exposure of the mutant to the ML exposure.

312 To examine the redox state of the photosynthetic apparatus, the pool of electron acceptors
313 downstream of PSII were evaluated. We quantified the photochemical efficiency (qL) of all strains
314 in LL and ML acclimated cells (**Fig. 4C**). The photosynthetic parameter qL indicates the redox
315 state of Q_A, the primary electron acceptor of the PSII reaction center. Assuming that Q_A and Q_B
316 are in equilibrium, qL would reflect the redox status of the PQ pool; a lower qL value indicates a
317 more reduced electron transport chain (Kramer et al., 2004). 1-qL positively correlates with the
318 PQ pool redox state. In LL-grown cells, 1-qL was significantly higher in *t3ko2* even at low level
319 illumination compared to that of WT and the rescued strain. For cells that had been acclimated to
320 ML (6 h and 24 h), 1-qL was 70% to near maximal for *t3ko2* even under low actinic light conditions

321 (e.g. 100 µmol photons m^{-2} s^{-1}), indicating a highly reduced PQ pool. In contrast, for WT and the
322 complemented strain, at the same light intensity (100 µmol photons m^{-2} s^{-1}), the 1-qL value attained
323 only ~20% of the maximum value (**Fig. 4C**). These results suggest that the PQ pool is more
324 reduced in the LL-acclimated *t3ko2* relative to the WT and *C_T3KO2* (**Fig. 4C**) and that there is a
325 much more pronounced reduction of this pool at all actinic light intensities in ML grown *t3ko2*.
326 These results suggest a limitation in electron flow downstream of the PQ pool in both LL and ML
327 grown *t3ko2*.

328 Moreover, we analyzed how fast PET becomes restricted following the transfer of LL-grown *t3ko2*,
329 *C_T3KO2* and WT cells to HL (400-450 µmol photons m^{-2} s^{-1}) by monitoring changes in the redox
330 state of the PQ pool. We observed that the PQ pool in *t3ko2* began to be more reduced than that of
331 WT cells and *C_T3KO2* immediately after 105 s of elevated illumination (**Fig. 4D**), which
332 becomes much more pronounced at longer times in the HL. These results suggest that PET can be
333 rapidly limited by diminished triose-P export from the chloroplast; elimination of CreTPT3 has a
334 strong impact on PET activity.

335 To determine if PSI was also impacted in the mutant cells, we analyzed PSI/P700
336 oxidation/reduction kinetics following exposure of LL-grown cells to ML in the presence of
337 DCMU (20 µM) and hydroxylamine (1 mM) to block a contribution of electrons from PSII. Levels
338 of photo-oxidized P700 following exposure to actinic light for 5 sec were similar in all LL-
339 acclimated strains (**Fig. 4E**). However, the level of photo-oxidized P700 in ML-acclimated cells
340 declined in the mutant to ~40-50% of that in WT and *C_T3KO2* cells (**Fig. 4E**), indicating that
341 PSI is more reduced in *t3ko2* after ML exposure. As shown in **Fig. 4F**, the oxidation rate of P700
342 following a dark to light transition was much slower in the ML-acclimated *t3ko2* compared to that
343 of WT. These results suggest that the mutant has a diminished level of available electron acceptors
344 on the acceptor side of PSI (relative to WT and *C_T3KO2*) after growth in ML.

345 **Inactivation of CreTPT3 dramatically affected cellular H_2O_2 accumulation and distribution**

346 To investigate the function of CreTPT3 in reducing or preventing the generation of oxidative stress,
347 we assayed ROS production in the mutant using the fluorescent probe CM-H2DCFDA which,
348 upon exposure to increasing ROS levels, is converted to the green-fluorescent molecule
349 dichlorofluorescein (DCF). DCF fluorescence was visualized by confocal microscopy. As shown
350 in **Fig. 5A** and **B**, ROS levels in the *t3ko2* mutant were markedly increased (~3-fold) after 48 h in

351 ML, while no difference in the ROS level was detected in WT cells.

352 For an alternative, dynamic method for evaluating redox changes in the chloroplast, we used the
353 redox sensitive green fluorescent protein roGFP2, which was targeted to the chloroplast stroma
354 (**Fig. 5C**, upper panel) and mitochondria (**Fig. 5C**, lower panel). roGFP2 monitors ratiometric
355 redox changes of glutathione, which reflects cellular ROS levels (Dorion et al., 2021; Vevea et al.,
356 2013). LL-acclimated WT cells and the *t3ko2* mutant exhibited similar levels of chloroplast roGFP
357 oxidation (**Fig. 5D**). Upon transfer of these cells to ML, the mutant showed a much greater increase
358 in chloroplast oxidative conditions, with a 5.0-fold increase after 1.5 h, and a 2.0-fold increase
359 after 6 h, which is 1.8- and 1.6-fold higher than the values measured in WT cells (**Fig. 5D**). As
360 triose-P is exported to the cytosol by CreTPT3, it could potentially be further metabolized and
361 donate redox equivalents to the mitochondrial electron transport chain and alter mitochondrial
362 ROS production. Therefore, we measured mitochondrial redox levels at different light intensities
363 in both WT and the *t3ko2* mutant using the roGFP2 sensor targeted to the mitochondrion. Upon a
364 LL to ML transition, neither WT nor *t3ko2* displayed a significant change in fluorescence from the
365 mitochondrial targeted roGFP (**Fig. 5E**). These results suggest that the mitochondrial redox level
366 is maintained after shifting either LL acclimated WT or *t3ko2* cells to ML. Overall, the inability
367 to export triose-P through CreTPT3 markedly increased the level of oxidative stress in the
368 chloroplast but not in the mitochondrion.

369 We also determined if the ROS accumulated in *t3ko2* is H_2O_2 and whether this molecule shows
370 differential accumulation in the different subcellular compartments; the analysis was based on the
371 use of a hypersensitive sensor of H_2O_2, roGFP2-Tsa2ΔCR, which was previously used for studies
372 of Chlamydomonas (Niemeyer et al., 2021). In this study, we monitored real-time accumulation
373 of the H_2O_2 in the stroma, cytosol, mitochondrion and nucleus following a 20 min exposure either
374 to HL or very low light (**Fig. 6A**). The *t3ko2* stromal H_2O_2 level increased rapidly within 2.5 min
375 and attained a 1.4-fold increase after 20 min of illumination with HL compared to the initial level
376 in LL (**Fig. 6B**). The stromal H_2O_2 levels in WT cells showed little change after being shifted to
377 HL, however, the level declined when the cells were shifted to 10 μmol photons m^{-2} s^{-1}, or very
378 low light. Notably, after 20 min in HL, the stroma of the *t3ko2* mutant accumulated ~1.6-fold more
379 H_2O_2 than that of the WT cells; *t3ko2* mutant cells in very low light accumulated a similar amount
380 of stromal H_2O_2 as WT cells after being exposed to HL (**Fig. 6B**). The cytosolic probe also

381 responded rapidly, with a 1.2-fold increase for WT and a 1.4-fold increase for the *t3ko2* mutant
382 (**Fig. 6C**); note that the initial levels of H_2O_2 prior to the transfer of the cells to HL or very low
383 light were much lower in the WT cells than in the mutant. The *t3ko2* cytosolic H_2O_2 level was
384 elevated relative to the level in WT cells by 2.1-fold after 20 min of illumination in HL (**Fig. 6C**).
385 We did not observe a significant change in H_2O_2 levels in the mitochondrion for either the WT or
386 the *t3ko2*mutant after the cells were shifted to the higher light intensity (**Fig. 6D**). Finally, the
387 *t3ko2* mutant already accumulated much higher levels of H_2O_2 in the nucleus in LL compared to
388 that in the WT cells, although both the mutant and WT did not show significant changes of H_2O_2
389 levels after HL exposure (**Fig. 6E**).

390 **Discussion**

391 **CreTPT3 is critical for maintaining intracellular partitioning of fixed carbon**

392 An Arabidopsis mutant for the chloroplast TPT was isolated 20 years ago (Schneider et al., 2002).
393 The growth of this mutant, which was designated *ape2*, was little affected under LL conditions
394 although its starch content was slightly elevated relative to that of WT Arabidopsis (Walters et al.,
395 2004). While *ape2* grew in HL, its growth was attenuated relative to WT Arabidopsis, although
396 there was no detectable change in starch accumulation (Walters et al., 2004). In potato, diminished
397 levels of chloroplast targeted TPT led to a 2-3-fold increase in starch accumulation; young
398 transgenic plants had a dwarf phenotype (Riesmeier et al., 1993). In comparison, the flux of fixed
399 carbon trafficked through CreTPT3 is absolutely critical for the growth of Chlamydomonas under
400 all light intensities tested, and it becomes essential for survival at the higher intensities (**Fig. 2**). In
401 addition to severe growth retardation, the *t3ko2* mutant exhibited a dramatic change in its carbon
402 partitioning. The starch content in *t3ko2* was markedly elevated in the mutant in both LL and ML
403 compared to WT cells, suggesting bottleneck in the export of fixed carbon in mutant cells, leading
404 to the storage of this carbon as starch and lipid (**Fig. 3A-D, Supplementary Fig. 7A**). In
405 Arabidopsis, elimination of the chloroplast targeted TPT1 protein did not significantly alter the
406 profiles of metabolites of either the CBBC or the glycolytic/gluconeogenic pathways (Hilgers et
407 al., 2018). In contrast, a Chlamydomonas mutant null for Cre*TPT3* exhibited a marked increase of
408 most metabolites associated with the CBBC and starch synthesis after exposure to either LL or
409 ML, indicating that triose-P exchange catalyzed by CreTPT3 was not readily compensated for by
410 alternative fixed carbon shuttles. CreTPT10, CrePPT2, CGL51, other translocators on the

411 chloroplast envelope that potentially use sugar-P molecules as substrates are unable to compensate
412 for the loss of CreTPT3 (**Supplementary Fig. 8B-D**).

413 In plants, the products of starch break-down can be routed out of chloroplasts by the MEX1 and
414 GlcT proteins. These translocators can compensate for the loss of TPT (Cho et al., 2011; Niittylä
415 et al., 2004; Walters et al., 2004). The Chlamydomonas chloroplast also likely contains MEX1,
416 which exhibited differential transport activities relative to that in vascular plants. Chlamydomonas
417 MEX1 can transport glucose and/or glucose phosphate across the envelope membrane, but there
418 is no strong evidence to show that it can export maltose as a *mex1* mutant did not accumulate
419 maltose or exhibit growth impairment (Findinier et al., 2017). Although the MEX1 transporter
420 cannot compensate for the loss of CreTPT3 in Chlamydomonas, we cannot rule out the possibility
421 that part of the accumulated starch in the Chlamydomonas *t3ko2* mutant can be mobilized in light,
422 with degradation products exported via MEX1.

423 The loss of chloroplast TPT function appears to have a more severe impact on Chlamydomonas
424 than on vascular plants. Land plants contain the entire glycolytic pathway in both the chloroplast
425 and cytosol while the pathway is partitioned between two compartments in Chlamydomonas; 90%
426 of the upper activities of the pathways(from F6P→ 3PG) was found to be associated with the
427 plastid while over 95% of the activities associated with the lower part of the pathway
428 (3PG→Pyruvate) appeared to be present in the cytosol (Klein, 1986; Rochaix et al., 1998)
429 Furthermore, for intact purified chloroplasts, almost 38% of the exported metabolites consist of 3-
430 PGA and DHAP (Rochaix et al., 1998). This compartmentalization likely requires CreTPT3,
431 which serves as the major carbon exporter from the chloroplast in Chlamydomonas in the light.
432 Investigation of the fluxes of specific carbon metabolites from the chloroplast under various
433 conditions in WT and the *tpt3* mutant is part of our current focus.

434 **CreTPT3, a safety valve allowing the acclimation of PET to light stress**

435 It was previously proposed that chloroplast TPTs could catalyze two potential reactions in the light
436 (**Fig. 7**) based on crystal structure analyses of TPT in the red algae (Lee et al., 2017a) and in vitro
437 assays using isolated spinach chloroplasts (Stocking and Larson, 1969): *i*) triose-P/Pi or *ii*) triose-
438 P/3-PGA exchange across the chloroplast inner envelope membrane. The former reaction can route
439 both carbon skeletons and reductants into the cytoplasm while importing Pi back into the
440 chloroplast for ATP regeneration. The latter reaction can import 3-PGA into the chloroplast in

441 exchange for triose-P (DHAP, GAP), which can serve as a substrate for the CBBC and allow for
442 ribulose 1,5-bisphosphate regeneration when it becomes depleted. The latter reaction also results
443 in the shuttling reductant (NAD(P)H) to the cytosol with zero net-carbon export. Indeed, in vitro,
444 TPT3 can actively transport both triose-P and 3-PGA in exchange for Pi (**Fig. 1**), suggesting that
445 TPT3 can potentially catalyze these two reactions and serve as a 'reductant shuttle' in addition to
446 a carbon shuttle. This exchange would eliminate excess reductant from the chloroplast, which
447 would help sustain photosynthetic electron flow.

448 Studies of photosynthetic activities of WT and *t3ko2* in both LL and ML support the idea that the
449 mutant is aberrant in its export of fixed carbon and reductant from the chloroplast. For LL-
450 acclimated *t3ko2* cells, the PQ pool (**Fig. 4C**) is much more reduced than in WT cells. However,
451 there is no loss of functions of either PSII or PSI activities (**Fig. 4A, B, E**) with the redox level and
452 oxidation rate of PSI comparable to that of the WT (**Fig. 4E, F**), suggesting that there is a reduced
453 rate of oxidation of the PQ pool. During ML exposure, the mutant stopped growing and, if placed
454 in HL, experienced severe bleaching (**Fig. 2E**). Furthermore, the highly reduced PQ pool and PSI
455 in ML-acclimated *t3ko2* (**Fig. 4C, E**) reflects a highly reduced PET system and the generation of
456 'over-flow' electrons. The slower oxidation rate of PSI in ML-acclimated *t3ko2* cells following
457 the dark to light transition during P700 measurement (**Fig. 4F**) along with the intracellular
458 accumulation of triose-P and 3-PGA indicates a block on the acceptor side of PSI. A defect in
459 routing carbon/reductants out of the chloroplast through CreTPT3 would cause hyper-
460 accumulation of reductant in the chloroplast, which would potentially result in a backup of PET.
461 The excess absorbed light energy by photosynthetic reaction centers can be dissipated either by
462 the export of fixed carbon (reaction: triose-P/Pi), which is coupled with reductant, or by shuttling
463 reductant out of chloroplasts that results in zero-net carbon export (reaction: malate/oxaloacetate
464 or triose-P/3-PGA exchange) (**Fig. 7**).

465 The malate-OAA shuttle represents another route that, under high redox stress, might have
466 partially compensated for the loss of the CreTPT3 by shuttling reductant from the chloroplast.
467 Intriguingly, malate levels in *t3ko2* were 4-fold lower than in WT cells (**Fig. 3E**, **G**). Moreover,
468 the expression of the plastidial malate dehydrogenases (Cre*MDH1* and Cre*MDH5*) were 3- to 6-
469 fold lower than that of the WT cells following a transition from LL to ML (**Supplementary Fig.**
470 **8E-F**), suggesting that the malate-OAA shuttle cannot compensate for a loss of CreTPT3 activity

471 in Chlamydomonas. Inactivation of triose-P/reductant export through CreTPT3 might have a
472 negative impact on the malate-OAA shuttle through metabolic rewiring. A previous study of
473 metabolic flux analysis during heterotrophic growth of Chlamydomonas showed that the TPT
474 shuttle is almost 10-fold more active than the malate-OAA shuttle (Boyle et al., 2017).

475 ***tpt3* mutant experiences oxidative stress**

476 In plants, the export of sugars and other molecules (redox/ROS, specific sugar levels) can serve as
477 signals that coordinate chloroplast and nuclear gene expression during acclimation to HL (Häusler
478 et al., 2014; Zirngibl et al., 2022). In our study, we probed the impact of impaired triose-P export
479 (*tpt3* mutant, *t3ko2*) on ROS production and accumulation in the different subcellular
480 compartments following exposure of the cells to ML or HL. In plant cells, H_2O_2 is produced as a
481 side-product of cellular processes including PET, mitochondrial respiration, and substrate level
482 oxidation (Cheeseman; Foyer and Noctor, 2016). While ROS stability is generally low, it can
483 accumulate in cells experiencing oxidative stress, with H_2O_2 being the most prevalent species that
484 functions as an important redox messenger (Li and Kim, 2022). Moreover, the trafficking of H_2O_2
485 into or out of different cellular compartments can trigger activation of other retrograde and
486 anterograde signals that may coordinate the activities among the compartments, including the
487 nucleus (Exposito-Rodriguez et al., 2017; Mittler et al., 2022; Shapiguzov et al., 2012). Upon
488 exposure to HL, the *t3ko2* mutant in Chlamydomonas accumulated more stromal H_2O_2 which
489 could diffuse rapidly out of the chloroplast and to the cytoplasm (**Fig. 6B, C**). Both stromal and
490 cytosolic H_2O_2 levels exhibited a similar increase, although it is still uncertain whether or not this
491 increase is solely dependent on H_2O_2 diffusion from the chloroplast stroma. It is unlikely that
492 mitochondria contribute to the increase in H_2O_2 in the *t3ko2* since exposing the mutant to elevated
493 light levels did not lead to accumulation of intramitochondrial H_2O_2 (**Fig. 6D**). However, an
494 increase in cytosolic H_2O_2 in the *t3ko2* mutant when exposed to either high or low light intensities
495 appears to influence H_2O_2 accumulation in the nucleus (**Fig. 6E**); the level of H_2O_2 in the cytoplasm
496 or nucleus of WT cells was not strongly impacted by the light conditions used in the experiments.
497 Such observations are consistent with previous reports demonstrating that the nuclear H_2O_2 level
498 was not significantly increased in WT Chlamydomonas cells exposed to HL (Niemeyer et al.,
499 2021), which suggest that the cytosol or the other organelles, such as the peroxisomes, might act
500 as a barrier that limits the intracellular diffusion of H_2O_2 into the nucleus. H_2O_2 transfer from the

501 chloroplast to the cytosol in the *t3ko2* mutant can potentially trigger retrograde signals that
502 modulate nuclear gene expressions, which in turn could ameliorate some of the negative effects of
503 ROS and elicit repair of the photosynthetic apparatus. A similar response may be elicited in WT
504 cells if the intensity of actinic light is increased to higher levels.

505 It has been shown that H_2O_2 can be synthesized in thylakoid membranes through the oxidation of
506 plastoquinol (PQH_2), suggesting a positive correlation between the redox state of the PQ pool and
507 the generation of H_2O_2 (Khorobrykh et al., 2015). This has become evident in both *Nicotiana*
508 *benthamiana* and Chlamydomonas based on the use of different H_2O_2 hypersensitive sensors
509 (Exposito-Rodriguez et al., 2017; Niemeyer et al., 2021). These two organisms have also been
510 shown to accumulate more stromal H_2O_2 in HL, and that this HL response is dependent on
511 photosynthesis. We observed this positive correlation between PQ pool reduction and the
512 generation of H_2O_2 in the *t3ko2* mutant. A more reduced PQ pool was observed in *t3ko2* relative
513 to the WT cells after a HL exposure of 105 s (**Fig. 4D)**. In parallel, there was a marked increase in
514 the stromal H_2O_2 level following 2.5 min of HL exposure (**Fig. 6B**). Therefore, hyper-reduction of
515 the PQ pool in the mutant likely results in elevated production of stromal H_2O_2, suggesting that
516 CreTPT3 can diminish H_2O_2 synthesis/accumulation and sustain a high rate of PET during
517 acclimation of the cells to HL; the protection by Cre*TPT3* likely reflects its ability to export fixed
518 carbon, relieving the redox pressure and formation of ROS in the chloroplast. Cre*TPT3* is the most
519 responsive/upregulated of the four Chlamydomonas, chloroplast localized *TPT* family genes
520 following exposure of the cells to nitrogen, sulfur or iron deprivation (**Supplementary Fig. 9 A-**
521 **C**), which reinforces the hypothesis that the ability to traffic fixed carbon from the chloroplast is
522 important not only for distributing carbon to other compartments of the cell, but potentially also
523 for relieving oxidative stress in the organelle. The isolated *tpt3* mutant represent an important
524 resource for investigating the dynamics of H_2O_2 synthesis and accumulation, as well as its role in
525 eliciting transcriptional and post-transcriptional control of gene expression.

526 As depicted in **Fig. 7**, we propose that various tiers of redox regulation are potentially responsible
527 for the differential physiological responses of Chlamydomonas *tpt3* knockout mutants. When
528 *t3ko2* cells are initially transferred from LL to ML, the triose-P pool and metabolites derived from
529 that pool accumulate in the mutant because of its reduced capacity to move triose-P out of the
530 chloroplast, which also causes reduced CBBC activity, hyper-reduction of PET and accumulation

531 of ROS (which would inhibit photosynthetic activity). The hyper-reduction of PET and
532 accumulation of carbon metabolites in the chloroplast of the mutants would activate AGPase
533 through allosteric regulation and by the Fdx/Trx (ferredoxin/thioredoxin) and NTRC (NADPH-
534 dependent thioredoxin reductase C) redox systems, which would result in starch hyper-
535 accumulation (Ballicora et al., 2000; Lepistö et al., 2013) (**Fig. 7**). Furthermore, increased ROS
536 accumulation in chloroplasts and the elevated redox state of PET would elicit the generation of
537 retrograde signals that mediate changes in expression of nuclear genes (Shapiguzov et al., 2012;
538 Suzuki et al., 2012; Wakao and Niyogi, 2021) and stimulate the synthesis of specific activities that
539 function to ameliorate the impact of the hyper-reduced state of the chloroplast resulting from a
540 compromised ability to export reductant and fixed carbon from the organelle (**Fig. 7**).

541

542 **Material and methods**

543 **Strains and culture conditions**

544 WT Chlamydomonas M10 (CC-4403, isogenic line derived from CC-124) was used as the parental
545 strain for the generation of knockout mutants. Cultures were routinely cultivated in growth
546 chambers (LED-41L2, Percival Scientific, Inc.) at 25°C with continuous shaking on an orbital
547 shaker (VWR OS-500 Shaker) at 120 rpm, in Tris-Acetate-Phosphate (TAP) medium (Harris,
548 2009). Cultures were illuminated with continuous cool white LEDs (LED-41L2, Percival
549 Scientific, Inc.) at low light (LL, 30 µmol photons m^{-2} s^{-1}). Experiments were mostly performed
550 with cells grown in the photoautotrophic medium TP (which is TAP medium without acetate), and
551 in TAP medium in some cases, at 25ºC, and sparged with air while being shaken at 120 rpm in a
552 growth chamber (LED-41L2, Percival Scientific, Inc.). For growth assays, cultures were
553 inoculated to a density of 0.02 at $OD_{750\ nm}$ (~1×10^5 cells/mL) in TP sparged with air under either
554 LL or moderate light (ML, 250-300 µmol photons m^{-2} s^{-1}) intensities. For spectrophotometric and
555 chlorophyll fluorescence analyses, the experimental design is described in **Supplementary Fig. 1**.
556 Growth assays on solid medium were performed with cultures spotted onto the medium at different
557 dilutions (as indicated in the text) and exposed to different light intensities; spot tests for
558 photoautotrophic growth were on TP agar plates and for mixotrophic growth on TAP agar plates.
559 Agar plates were incubated for 7 d under either LL or ML (cool white LED) at 25°C.

560 **Reconstitution into liposomes and transport assays**

561 The procedures for the construction and expression of CreTPT3 in yeast are described in
562 supplemental information (SI). For uptake studies, yeast membranes from cells with and without
563 recombinant His-tagged CreTPT3 were enriched and reconstituted into 3% (w/v) L-alpha-
564 phosphatidylcholine using a freeze-thaw-sonication procedure (Linka et al., 2008). The
565 reconstituted liposomes were preloaded with 30 mM Pi or phosphorylated metabolites to be tested
566 as potential transport substrates. As a negative control for antiport activity, liposomes were also
567 generated without metabolite preloading. The external counter-exchange substrate was removed
568 via gel filtration on Sephadex G-25M columns (GE Healthcare). Transport assays were initiated
569 by adding 0.25 mM [alpha-^{32}P]-phosphoric acid (6,000 Ci/mmol) to the medium bathing the
570 liposomes and performed as previously described by Linka et al. (2008). Measurements of Km for
571 Pi and competitive inhibition constants (Ki) are described in supplemental information (SI)

572 **Vector construction, transformation and subcellular localization**

573 The pRam118_VENUS plasmid, which harbors the VENUS gene and the *AphVII* cassette (confers
574 resistance to hygromycin) (Cre01.g045550)(Kaye et al., 2019), was used to express Cre*TPT3*
575 (Cre01.g045550). The step-by-step description is in supplemental information (SI). Following
576 construction, 2-4 µg of the plasmid was linearized and added to 250 µL of a cell suspension at a
577 concentration of ~3×10^8 cells/mL per reaction. The GeneArt MAX Efficiency Transformation
578 Reagent for algae (Invitrogen) was used for introducing the plasmid into the algal cells by
579 electroporation according to the instructions provided by the manufacturer. Transformants were
580 selected on solid TAP medium containing hygromycin (10 µg/mL; Enzo Life).

581 Drug resistant transformants were visualized for VENUS fluorescence as previously described
582 (Kaye et al., 2019). In brief, transgenic cell lines resistant to hygromycin were screened for
583 VENUS fluorescence using a microplate reader (Infinite M1000; TECAN). Excitation and
584 emission settings were as follows: VENUS, excitation 515nm, bandwidth 12 nm and emission 550
585 nm, bandwidth 12 nm; chlorophyll excitation 440 nm, bandwidth 9 nm and emission 680 nm,
586 bandwidth 20 nm. The TCS SP8 confocal laser-scanning microscope (Leica) was used to visualize
587 the VENUS fluorescence signal (Kaye et al., 2019).

588 **CRISPR-Cas9 mediated mutagenesis**

589 *Chlamydomonas reinhardtii* WT strain CC-124 was used for mutant generation. WT cells were
590 cultured under continuous light (50 µmol photons m^{-2} s^{-1}) for 2 d to a density of 3-5×10^6 cells/mL.
591 The cells were then concentrated to 2×10^8 cells/mL in 0.5×TAP supplemented with 80 mM sucrose.
592 Two single guide RNAs (sgRNA) were designed by CHOPCHOP and synthesized by Integrated
593 DNA Technologies (IDT). The sequences of the generated sgRNA are: *TPT3*-sg1 (5′-
594 CGCUGGGCGTCACUUCCCGGCGG-3′) for editing exon 1 and *TPT3*-sg2 (5′-
595 AAGGCCGCUAUCGCCAACGUGGG-3′) for editing of exon 7. The protocol for disruption of
596 Cre*TPT3* (Cre01.g045550) was adapted from (Findinier et al., 2019) and is described in (SI).

597 **Complementation of mutants *tpt3* mutants**

598 Mutant strains were transformed with the linearized plasmid pRam118_CreTPT3 plasmid.
599 Transformed cells were selected in ML and then screened for VENUS fluorescence. Colonies
600 containing VENUS and an *AphVII* cassette knock-in at the Cas9 targeted site were examined for

601 accumulation of the CreTPT3 protein by immunoblots using CreTPT3 antibody generated by
602 GenScript USA Inc (Piscataway, USA). Colonies of immuno-positive cells were subjected to
603 growth complementation assays using spot tests under ML on either solid TAP or TP medium.

604 **P700 activity measurements**

605 Absorbance spectroscopy to measure P700 activity was performed in dark-adapted liquid cultures
606 (15 µg/mL chlorophyll, in 20 mM HEPES-KOH, pH 7.2, and 10% ficoll) using a JTS-100
607 spectrophotometer (SpectroLogiX, TN) as previously described (Clowez et al., 2021). Actinic light
608 was provided by an orange LED (165 µmol photons m^{-2} s^{-1}) for PSI oxidation, followed by a
609 saturating pulse and dark incubation. 20 µM DCMU and 1 mM hydroxylamine were added to the
610 cell suspension to inhibit linear electron flow (LEF) prior to the measurement. P700 activity was
611 measured by monitoring the absorbance at 705 nm (interference filter 6 nm FWHM was used to
612 create a narrow excitation beam); the absorbance at 740 nm was used to correct for an unspecific
613 contribution to the 705 nm signal.

614 **Chlorophyll fluorescence analysis**

615 Chlorophyll fluorescence, used to evaluate photosynthetic electron transport, was measured with
616 a DUAL PAM-100 fluorometer. Cells were acclimated in the dark for 20 min prior to illumination
617 at increasing light intensities (0, 10, 50, 100, 200, 400, 800, 1000, 1200 µmol photons m^{-2} s^{-1}) for
618 2 min at each intensity, or at a constant intensity of 450 µmol photons m^{-2} s^{-1} for 10 min to evaluate
619 1-qL. 1 mM CO_2 ($NaHCO_3$) was added to the reaction mix as an electron acceptor for the CBBC.

620 **ROS measurements and roGFP2 imaging analysis**

621 All strains were grown photoautotrophically under LL for 16-24 h. After dilution with fresh
622 medium, the cultures were transferred to ML and then stained with CM-H2DCFDA (Thermo
623 Fisher Scientific) as described in (Kong et al., 2018) for detecting ROS. A step-by-step protocol
624 is given in (SI).

625 Constructs containing chloroplast or mitochondria targeting sequences (Crozet et al., 2018) fused
626 to codon-optimized roGFP2 (Vevea et al., 2013) were transformed into WT and mutant strains.
627 Cells were cultured as shown in **Supplementary Fig. 1**. Signals from the transformed lines were
628 visualized using a TCS SP8 confocal laser-scanning microscope (Leica). roGFP2 signals were

629 collected and analyzed as previously described (Vevea et al., 2013). Using the sequential setup of
630 the SP8, roGFP2 signals were collected at the emission wavelength of 510-550 nm immediately
631 following excitation at 405 nm and 488 nm (Vevea et al., 2013). The degree of roGFP2 oxidation
632 was analyzed as the ratio of the emission signals after excitation at 405 nm and 488 nm (Vevea et
633 al., 2013).

634 Plasmids harboring H_2O_2 roGFP2-Tsa2ΔCR sensors (Niemeyer et al., 2021) were obtained from
635 the Chlamydomonas Resource Center (https://www.chlamycollection.org/) (**Supplementary**
636 **Table. 2)**. Cells in which roGFP2-Tsa2ΔCR was targeted to the stroma, cytosol, mitochondrial
637 matrix, or nucleus were initially grown in LL in TAP to exponential growth phase. Cells were then
638 grown in TP in LL for 2 h and shifted either to HL or very low light (10 µmol photons m^{-2} s^{-1}).
639 The oxidation state of the sensor was trapped by the addition of N-Ethylmaleimide (NEM) (Sigma
640 Aldrich) and roGFP2 fluorescence was measured in a plate reader (Infinite M1000; TECAN).
641 Signals were detected using the excitation wavelengths of 410 and 488 nm, and the emission
642 wavelength of 514 nm. The degree of sensor oxidation (OxD) was calculated as described in
643 (Niemeyer et al., 2021).

644 **Photosynthesis-Irradiance curve**

645 Photosynthesis-Irradiance curves were measured using a custom Pt-Ag/AgCl polarographic
646 electrode system (ALGI) with a water jacketed (for temperature-control), 1 mL glass reaction
647 chamber. A step-by-step protocol is provided in SI.

648 **Starch and TAG quantification**

649 Cells were grown under LL to mid-exponential phase, diluted to 0.5 µg/mL chlorophyll with fresh
650 medium and transferred to and then grown in ML for 24 h or more, as indicated. Starch was
651 measured according to (Klein and Betz, 1978), , with slight modification (and see SI).
652 Triacylglycerol (TAG) levels were estimated by a fluorometric assay using the dye Nile Red
653 (Thermo Fisher)(Yu et al., 2009). A Nile Red solution (500 µg/mL in acetone) was added to 1 mL
654 of the cell suspensions to a final concentration of 0.5 µg/mL. Samples were then incubated at room
655 temperature for 30 min, and the Nile Red fluorescence emission quantified at 575 nm following
656 excitation at 530 nm using a microplate reader (Infinite M1000; TECAN).

657

658 **Metabolic analysis**

659 Cells grown in LL were shifted to ML for 45 min or 6 h, as indicated. 45 mL of culture was rapidly
660 quenched in cold saline solution (-2 to -3°C), extracted using cold methanol and then analyzed by
661 LC-MS/MS. Quenching and analysis of metabolites were performed, with modifications,
662 according to (Sake et al., 2020). A step-by-step protocol is described in (SI). Metabolite extracts
663 were analyzed using LC-MS/MS adapted from (Young et al., 2011). A Phenomenex 150 mm x 2
664 mm Synergi Hydro-RP column was used on an Agilent 1200 Series HPLC system coupled to an
665 AB Sciex 5500 QTRAP system. LC was performed with a liquid injection volume of 20 µL and a
666 gradient elution with 10 mM tributylamine and 15 mM acetic acid (aqueous phase) in acetonitrile
667 (organic phase) (reagent B) at a constant flow rate of 0.3 mL/min, and a constant temperature of
668 40°C. The gradient profile of the organic phase is as follows: 0% B (0 min), 8% B (10 min), 16%
669 B (15 min), 30%B (16.5 min), 30% B (19 min), 90% B (21.5 min), 90% B (28 min), 0% B (28.5
670 min), and 0% B (35 min). MS analysis was performed in negative mode using a multiple reaction
671 monitoring (MRM) acquisition method. Data acquisition was performed on the ABSciex Analyst
672 1.7 software. Absolute quantification of intracellular metabolites was performed using the
673 quantitation mode on the Analyst software. All chemicals used for metabolite extraction and LC-
674 MS/MS analysis were Optima grade reagents.

675

Acknowledgments:

WH thanks Dr. Masayuki Onishi for advice on the generation of CRISPR mutants and Adrien Burlacot for help with PQ pool measurements.

Funding:

This project has supported by DOE award DE-SC0019417 to ARG. WH was supported solely by a grant from the US Department of Energy, Office of Science, Basic Energy Systems (DE-SC0019417). AK and MCP were supported solely by a grant from the US Department of Energy, Office of Science, Basic Energy Systems (DE-SC0019341 to MP). NB and MM were supported by US Department of Energy, Office of Science, Office of Biological and Environmental Research (BER), (DE-SC0018301 to NB). NL and AP were supported by German Research Foundations (DFG Grant LI1781/2-2). BR was supported by National Science Foundation (Award Number : 1645164). RGK and JF were supported by the Department of Plant Biology of the Carnegie Institution for Science. PR was supported by Human Frontier Science Program (HFSP) RGP0046/2018 (to ARG).

Author contributions:

WH, AK, ARG and MP conceptualized the study. WH generated the CRISPR mutants as well as the complemented strain, localized the TPT3 protein, performed respiration measurements, measured the reduction level of PQ pool. AK performed the experiments of photosynthetic O_2 evolution, extraction of samples for LC-MS/MS, data analysis of LC-MS/MS. AP and NL performed the reconstitution into liposomes and transport activity assays. MM and NB performed LC-MS/MS and analyses of metabolite data. WH and YW analyzed the redox status in the cell. BR performed data mining for transcriptome and the Nile red staining. JF and NF analyzed starch changes upon transition from LL to ML. WH, PR and ARG analyzed PSI and PSII activities. JF and BR constructed roGFP2 associated vectors. ARG, MP, AK, NL, NB, AP, MM and all the other authors helped with revising and finalizing the manuscript.

Competing interests:

All other authors declare they have no competing interests.

Data and materials availability:

All data are available in the main text or the supplementary materials.

References

Ballicora, M.A., Frueauf, J.B., Fu, Y., Schürmann, P., and Preiss, J. (2000). Activation of the potato tuber ADP-glucose pyrophosphorylase by thioredoxin. J. Biol. Chem. *275*, 1315–1320. https://doi.org/10.1074/jbc.275.2.1315.

Bhatt, P., Bhandari, G., Turco, R.F., Aminikhoei, Z., Bhatt, K., and Simsek, H. (2022). Algae in wastewater treatment, mechanism, and application of biomass for production of value-added product. Environ. Pollut. *309*, 119688. https://doi.org/10.1016/j.envpol.2022.119688.

Boschetti, A., and Schmid, K. (1998). Energy Supply for ATP-Synthase Deficient Chloroplasts of *Chlamydomonas reinhardii*. Plant Cell Physiol. *39*, 160–168. https://doi.org/10.1093/oxfordjournals.pcp.a029353.

Boyle, N.R., Sengupta, N., and Morgan, J.A. (2017). Metabolic flux analysis of heterotrophic growth in *Chlamydomonas reinhardtii*. PLoS One *12*, e0177292. https://doi.org/10.1371/journal.pone.0177292.

Chaux, F., Burlacot, A., Mekhalfi, M., Auroy, P., Blangy, S., Richaud, P., and Peltier, G. (2017). Flavodiiron proteins promote fast and transient O_2 photoreduction in Chlamydomonas. Plant Physiol. *174*, 1825–1836. https://doi.org/10.1104/pp.17.00421.

Cheeseman, J.M. Hydrogen peroxide and plant stress: A challenging relationship.

Cho, M.-H., Lim, H., Shin, D.H., Jeon, J.-S., Bhoo, S.H., Park, Y.-I., and Hahn, T.-R. (2011). Role of the plastidic glucose translocator in the export of starch degradation products from the chloroplasts in *Arabidopsis thaliana*. New Phytol. *190*, 101–112. https://doi.org/10.1111/j.1469-8137.2010.03580.x.

Clowez, S., Renicke, C., Pringle, J.R., and Grossman, A.R. (2021). Impact of menthol on growth and photosynthetic function of *Breviolum minutum* (Dinoflagellata, Dinophyceae, Symbiodiniaceae) and Interactions with its Aiptasia Host. J. Phycol. *57*, 245–257. https://doi.org/10.1111/jpy.13081.

Crozet, P., Navarro, F.J., Willmund, F., Mehrshahi, P., Bakowski, K., Lauersen, K.J., Pérez-Pérez, M.-E., Auroy, P., Gorchs Rovira, A., Sauret-Gueto, S., et al. (2018). Birth of a photosynthetic chassis: A MoClo toolkit enabling synthetic biology in the microalga *Chlamydomonas reinhardtii*. ACS Synth. Biol. *7*, 2074–2086. https://doi.org/10.1021/acssynbio.8b00251.

Dorion, S., Ouellet, J.C., and Rivoal, J. (2021). Glutathione metabolism in plants under stress: beyond reactive oxygen species detoxification. Metabolites *11*, 641. https://doi.org/10.3390/metabo11090641.

Eicks, M., Maurino, V., Knappe, S., Flügge, U.-I., and Fischer, K. (2002). The plastidic pentose phosphate translocator represents a link between the cytosolic and the plastidic pentose phosphate pathways in plants. Plant Physiol. *128*, 512–522. https://doi.org/10.1104/pp.010576.

742 Exposito-Rodriguez, M., Laissue, P.P., Yvon-Durocher, G., Smirnoff, N., and Mullineaux, P.M.
743 (2017). Photosynthesis-dependent H_2O_2 transfer from chloroplasts to nuclei provides a high-light
744 signalling mechanism. Nat. Commun. *8*, 49. https://doi.org/10.1038/s41467-017-00074-w.

745 Findinier, J., Tunçay, H., Schulz-Raffelt, M., Deschamps, P., Spriet, C., Lacroix, J.-M., Duchêne,
746 T., Szydlowski, N., Li-Beisson, Y., Peltier, G., et al. (2017). The Chlamydomonas *mex1* mutant
747 shows impaired starch mobilization without maltose accumulation. J. Exp. Bot. *68*, 5177–5189.
748 https://doi.org/10.1093/jxb/erx343.

749 Findinier, J., Delevoye, C., and Cohen, M.M. (2019). The dynamin-like protein Fzl promotes
750 thylakoid fusion and resistance to light stress in *Chlamydomonas reinhardtii*. PLoS Genet. *15*,
751 e1008047. https://doi.org/10.1371/journal.pgen.1008047.

752 Fischer, K., Kammerer, B., Gutensohn, M., Arbinger, B., Weber, A., Hausler, R.E., and Flugge,
753 U.-I. (1997). A new class of plastidic phosphate translocators: A putative link between primary
754 and secondary metabolism by the phosphoenolpyruvate/phosphate antiporter. Plant Cell *9*, 453.
755 https://doi.org/10.2307/3870494.

756 Fliege, R., Flügge, U.-I., Werdan, K., and Heldt, H.W. (1978). Specific transport of inorganic
757 phosphate, 3-phosphoglycerate and triosephosphates across the inner membrane of the envelope
758 in spinach chloroplasts. Biochim. Biophys. Acta Bioenerg. *502*, 232–247.
759 https://doi.org/10.1016/0005-2728(78)90045-2.

760 Flügge, U.I., Fischer, K., Gross, A., Sebald, W., Lottspeich, F., and Eckerskorn, C. (1989). The
761 triose phosphate-3-phosphoglycerate-phosphate translocator from spinach chloroplasts:
762 nucleotide sequence of a full-length cDNA clone and import of the in vitro synthesized precursor
763 protein into chloroplasts. EMBO J. *8*, 39–46. .

764 Foyer, C.H., and Noctor, G. (2016). Stress-triggered redox signalling: what's in pROSpect? Plant
765 Cell Environ. *39*, 951–964. https://doi.org/10.1111/pce.12621.

766 Ge, F., Huang, W., Chen, Z., Zhang, C., Xiong, Q., Bowler, C., Yang, J., Xu, J., and Hu, H. (2014).
767 Methylcrotonyl-CoA carboxylase regulates triacylglycerol accumulation in the model diatom
768 *Phaeodactylum tricornutum*. Plant Cell *26*, 1681–1697. https://doi.org/10.1105/tpc.114.124982.

769 Gibson, D.G., Young, L., Chuang, R.-Y., Venter, J.C., Hutchison, C.A., 3rd, and Smith, H.O.
770 (2009). Enzymatic assembly of DNA molecules up to several hundred kilobases. Nat. Methods *6*,
771 343–345. https://doi.org/10.1038/nmeth.1318.

772 Gietz, R.D., and Schiestl, R.H. (2007). High-efficiency yeast transformation using the LiAc/SS
773 carrier DNA/PEG method. Nat. Protoc. *2*, 31–34. https://doi.org/10.1038/nprot.2007.13.

774 González-Ballester, D., Casero, D., Cokus, S., Pellegrini, M., Merchant, S.S., and Grossman, A.R.
775 (2010). RNA-seq analysis of sulfur-deprived Chlamydomonas cells reveals aspects of acclimation
776 critical for cell survival. Plant Cell *22*, 2058–2084. https://doi.org/10.1105/tpc.109.071167.

Haferkamp, I., Deschamps, P., Ast, M., Jeblick, W., Maier, U., Ball, S., and Neuhaus, H.E. (2006). Molecular and biochemical analysis of periplastidial starch metabolism in the cryptophyte *Guillardia theta*. Eukaryot. Cell *5*, 964–971. https://doi.org/10.1128/EC.00381-05.

Harris, E.H. (2009). Chlamydomonas sourcebook: Introduction to Chlamydomonas and its laboratory use (Academic Press).

Häusler, R.E., Schlieben, N.H., Schulz, B., and Flügge, U.I. (1998). Compensation of decreased triose phosphate/phosphate translocator activity by accelerated starch turnover and glucose transport in transgenic tobacco. Planta *204*, 366–376. https://doi.org/10.1007/s004250050268.

Häusler, R.E., Heinrichs, L., Schmitz, J., and Flügge, U.-I. (2014). How sugars might coordinate chloroplast and nuclear gene expression during acclimation to high light intensities. Mol. Plant *7*, 1121–1137. https://doi.org/10.1093/mp/ssu064.

Hilgers, E.J.A., Schöttler, M.A., Mettler-Altmann, T., Krueger, S., Dörmann, P., Eicks, M., Flügge, U.-I., and Häusler, R.E. (2018). The combined loss of triose phosphate and xylulose 5-Phosphate/Phosphate translocators leads to severe growth retardation and impaired photosynthesis in *Arabidopsis thaliana* tpt/xpt double mutants. Front. Plant Sci. *9*, 1331. https://doi.org/10.3389/fpls.2018.01331.

Houille-Vernes, L., Rappaport, F., Wollman, F.-A., Alric, J., and Johnson, X. (2011). Plastid terminal oxidase 2 (PTOX2) is the major oxidase involved in chlororespiration in Chlamydomonas. Proc. Natl. Acad. Sci. U. S. A. *108*, 20820–20825. https://doi.org/10.1073/pnas.1110518109.

Huang, W., Haferkamp, I., Lepetit, B., Molchanova, M., Hou, S., Jeblick, W., Río Bártulos, C., and Kroth, P.G. (2018). Reduced vacuolar β-1,3-glucan synthesis affects carbohydrate metabolism as well as plastid homeostasis and structure in *Phaeodactylum tricornutum*. Proc. Natl. Acad. Sci. U. S. A. *115*, 4791–4796. https://doi.org/10.1073/pnas.1719274115.

Jack, D.L., Yang, N.M., and Saier, M.H., Jr (2001). The drug/metabolite transporter superfamily. Eur. J. Biochem. *268*, 3620–3639. https://doi.org/10.1046/j.1432-1327.2001.02265.x.

Johnson, X., and Alric, J. (2013). Central carbon metabolism and electron transport in *Chlamydomonas reinhardtii*: metabolic constraints for carbon partitioning between oil and starch. Eukaryot. Cell *12*, 776–793. https://doi.org/10.1128/EC.00318-12.

Jokel, M., Johnson, X., Peltier, G., Aro, E.-M., and Allahverdiyeva, Y. (2018). Hunting the main player enabling *Chlamydomonas reinhardtii* growth under fluctuating light. Plant J. *94*, 822–835. https://doi.org/10.1111/tpj.13897.

Kammerer, B., Fischer, K., Hilpert, B., Schubert, S., Gutensohn, M., Weber, A., and Flügge, U.I. (1998). Molecular characterization of a carbon transporter in plastids from heterotrophic tissues: the glucose 6-phosphate/phosphate antiporter. Plant Cell *10*, 105–117. https://doi.org/10.1105/tpc.10.1.105.

812 Kaye, Y., Huang, W., Clowez, S., Saroussi, S., Idoine, A., Sanz-Luque, E., and Grossman, A.R.
813 (2019). The mitochondrial alternative oxidase from *Chlamydomonas reinhardtii* enables survival
814 in high light. J. Biol. Chem. *294*, 1380–1395. https://doi.org/10.1074/jbc.RA118.004667.

815 Khan, M.I., Shin, J.H., and Kim, J.D. (2018). The promising future of microalgae: current status,
816 challenges, and optimization of a sustainable and renewable industry for biofuels, feed, and other
817 products. Microb. Cell Fact. *17*, 36. https://doi.org/10.1186/s12934-018-0879-x.

818 Khorobrykh, S.A., Karonen, M., and Tyystjärvi, E. (2015). Experimental evidence suggesting that
819 H_2O_2 is produced within the thylakoid membrane in a reaction between plastoquinol and singlet
820 oxygen. FEBS Lett. *589*, 779–786. https://doi.org/10.1016/j.febslet.2015.02.011.

821 Klein, U. (1986). Compartmentation of glycolysis and of the oxidative pentose-phosphate pathway
822 in *Chlamydomonas reinhardii*. Planta *167*, 81–86. https://doi.org/10.1007/BF00446372.

823 Klein, U., and Betz, A. (1978). Fermentative metabolism of hydrogen-evolving *Chlamydomonas*
824 *moewusii*. Plant Physiol. *61*, 953–956. https://doi.org/10.1104/pp.61.6.953.

825 Klöck, G., and Kreuzberg, K. (1991). Compartmented metabolite pools in protoplasts from the
826 green alga *Chlamydomonas reinhardtii*: changes after transition from aerobiosis to anaerobiosis in
827 the dark. Biochim. Biophys. Acta *1073*, 410–415. https://doi.org/10.1016/0304-4165(91)90150-f.

828 Knappe, S., Flügge, U.-I., and Fischer, K. (2003). Analysis of the plastidic phosphate translocator
829 gene family in Arabidopsis and identification of new phosphate translocator-homologous
830 transporters, classified by their putative substrate-binding site. Plant Physiol. *131*, 1178–1190.
831 https://doi.org/10.1104/pp.016519.

832 Kong, F., Burlacot, A., Liang, Y., Légeret, B., Alseekh, S., Brotman, Y., Fernie, A.R., Krieger-
833 Liszkay, A., Beisson, F., Peltier, G., et al. (2018). Interorganelle communication: peroxisomal
834 MALATE DEHYDROGENASE2 connects lipid catabolism to photosynthesis through redox
835 coupling in Chlamydomonas. Plant Cell *30*, 1824–1847. https://doi.org/10.1105/tpc.18.00361.

836 Kramer, D.M., Johnson, G., Kiirats, O., and Edwards, G.E. (2004). New fluorescence parameters
837 for the determination of QA redox state and excitation energy fluxes. Photosynth. Res. *79*, 209.
838 https://doi.org/10.1023/B:PRES.0000015391.99477.0d.

839 Krishnan, A., Kumaraswamy, G.K., Vinyard, D.J., Gu, H., Ananyev, G., Posewitz, M.C., and
840 Dismukes, G.C. (2015). Metabolic and photosynthetic consequences of blocking starch
841 biosynthesis in the green alga *Chlamydomonas reinhardtii sta6* mutant. Plant J. *81*, 947–960.
842 https://doi.org/10.1111/tpj.12783.

843 Lee, S.-K., Eom, J.-S., Voll, L.M., Prasch, C.M., Park, Y.-I., Hahn, T.-R., Ha, S.-H., An, G., and
844 Jeon, J.-S. (2014). Analysis of a triose phosphate/phosphate translocator-deficient mutant reveals
845 a limited capacity for starch synthesis in rice leaves. Mol. Plant *7*, 1705–1708.
846 https://doi.org/10.1093/mp/ssu082.

847 Lee, Y., Nishizawa, T., Takemoto, M., Kumazaki, K., Yamashita, K., Hirata, K., Minoda, A.,
848 Nagatoishi, S., Tsumoto, K., Ishitani, R., et al. (2017a). Structure of the triose-

849 phosphate/phosphate translocator reveals the basis of substrate specificity. Nat Plants *3*, 825–832.
850 https://doi.org/10.1038/s41477-017-0022-8.

851 Lee, Y., Nishizawa, T., Takemoto, M., Kumazaki, K., Yamashita, K., Hirata, K., Minoda, A.,
852 Nagatoishi, S., Tsumoto, K., Ishitani, R., et al. (2017b). Crystal structure of the triose-
853 phosphate/phosphate translocator in complex with inorganic phosphate.
854 https://doi.org/10.2210/pdb5y78/pdb.

855 Lepistö, A., Pakula, E., Toivola, J., Krieger-Liszkay, A., Vignols, F., and Rintamäki, E. (2013).
856 Deletion of chloroplast NADPH-dependent thioredoxin reductase results in inability to regulate
857 starch synthesis and causes stunted growth under short-day photoperiods. J. Exp. Bot. *64*, 3843–
858 3854. https://doi.org/10.1093/jxb/ert216.

859 Li, M., and Kim, C. (2022). Chloroplast ROS and stress signaling. Plant Commun *3*, 100264.
860 https://doi.org/10.1016/j.xplc.2021.100264.

861 Lim, L., Linka, M., Mullin, K.A., Weber, A.P.M., and McFadden, G.I. (2010). The carbon and
862 energy sources of the non-photosynthetic plastid in the malaria parasite. FEBS Lett. *584*, 549–554.
863 https://doi.org/10.1016/j.febslet.2009.11.097.

864 Linka, M., Jamai, A., and Weber, A.P.M. (2008). Functional characterization of the plastidic
865 phosphate translocator gene family from the thermo-acidophilic red alga *Galdieria sulphuraria*
866 reveals specific adaptations of primary carbon partitioning in green plants and red algae. Plant
867 Physiol. *148*, 1487–1496. https://doi.org/10.1104/pp.108.129478.

868 Loddenkötter, B., Kammerer, B., Fischer, K., and Flügge, U.I. (1993). Expression of the functional
869 mature chloroplast triose phosphate translocator in yeast internal membranes and purification of
870 the histidine-tagged protein by a single metal-affinity chromatography step. Proc. Natl. Acad. Sci.
871 U. S. A. *90*, 2155–2159. https://doi.org/10.1073/pnas.90.6.2155.

872 Mittler, R., Zandalinas, S.I., Fichman, Y., and Van Breusegem, F. (2022). Reactive oxygen species
873 signalling in plant stress responses. Nat. Rev. Mol. Cell Biol. *23*, 663–679.
874 https://doi.org/10.1038/s41580-022-00499-2.

875 Moog, D., Nozawa, A., Tozawa, Y., and Kamikawa, R. (2020). Substrate specificity of plastid
876 phosphate transporters in a non-photosynthetic diatom and its implication in evolution of red alga-
877 derived complex plastids. Sci. Rep. *10*, 1167. https://doi.org/10.1038/s41598-020-58082-8.

878 Ngan, C.Y., Wong, C.-H., Choi, C., Yoshinaga, Y., Louie, K., Jia, J., Chen, C., Bowen, B., Cheng,
879 H., Leonelli, L., et al. (2015). Lineage-specific chromatin signatures reveal a regulator of lipid
880 metabolism in microalgae. Nat Plants *1*, 15107. https://doi.org/10.1038/nplants.2015.107.

881 Niemeyer, J., Scheuring, D., Oestreicher, J., Morgan, B., and Schroda, M. (2021). Real-time
882 monitoring of subcellular H_2O_2 distribution in *Chlamydomonas reinhardtii*. Plant Cell *33*, 2935–
883 2949. https://doi.org/10.1093/plcell/koab176.

884 Niittylä, T., Messerli, G., Trevisan, M., Chen, J., Smith, A.M., and Zeeman, S.C. (2004). A
885 previously unknown maltose transporter essential for starch degradation in leaves. Science *303*,
886 87–89. https://doi.org/10.1126/science.1091811.

887 Plaxton, W.C. (1996). The organization and regulation of plant glycolysis. Annu. Rev. Plant
888 Physiol. Plant Mol. Biol. *47*, 185–214. https://doi.org/10.1146/annurev.arplant.47.1.185.

889 Raghavendra, A.S., and Padmasree, K. (2003). Beneficial interactions of mitochondrial
890 metabolism with photosynthetic carbon assimilation. Trends Plant Sci. *8*, 546–553.
891 https://doi.org/10.1016/j.tplants.2003.09.015.

892 Riesmeier, J.W., Flügge, U.I., Schulz, B., Heineke, D., Heldt, H.W., Willmitzer, L., and Frommer,
893 W.B. (1993). Antisense repression of the chloroplast triose phosphate translocator affects carbon
894 partitioning in transgenic potato plants. Proc. Natl. Acad. Sci. U. S. A. *90*, 6160–6164.
895 https://doi.org/10.1073/pnas.90.13.6160.

896 Rochaix, J.-D., Goldschmidt-Clermont, M., and Merchant, S. (1998). The molecular biology of
897 chloroplasts and mitochondria in Chlamydomonas (Plenum Publishing Corporation).

898 Sake, C.L., Newman, D.M., and Boyle, N.R. (2020). Evaluation of quenching methods for
899 metabolite recovery in photoautotrophic *Synechococcus sp*. PCC 7002. Biotechnol. Prog. *36*,
900 e3015. https://doi.org/10.1002/btpr.3015.

901 Saroussi, S., Sanz-Luque, E., Kim, R.G., and Grossman, A.R. (2017). Nutrient scavenging and
902 energy management: acclimation responses in nitrogen and sulfur deprived Chlamydomonas. Curr.
903 Opin. Plant Biol. *39*, 114–122. https://doi.org/10.1016/j.pbi.2017.06.002.

904 Schneider, A., Häusler, R.E., Kolukisaoglu, Ü., Kunze, R., Van der Graaff, E., Schwacke, R.,
905 Catoni, E., Desimone, M., and Flügge, U.I. (2002). An Arabidopsis thaliana knock-out mutant of
906 the chloroplast triose phosphate/phosphate translocator is severely compromised only when starch
907 synthesis, but not starch mobilisation is abolished. Plant Journal https://doi.org/10.1046/j.1365-
908 313X.2002.01460.x.

909 Shapiguzov, A., Vainonen, J.P., Wrzaczek, M., and Kangasjärvi, J. (2012). ROS-talk - how the
910 apoplast, the chloroplast, and the nucleus get the message through. Front. Plant Sci. *3*, 292.
911 https://doi.org/10.3389/fpls.2012.00292.

912 Stocking, C.R., and Larson, S. (1969). A chloroplast cytoplasmic shuttle and the reduction of
913 extraplastid NAD. Biochem. Biophys. Res. Commun. *37*, 278–282. https://doi.org/10.1016/0006-
914 291x(69)90731-1.

915 Strenkert, D., Schmollinger, S., Gallaher, S.D., Salomé, P.A., Purvine, S.O., Nicora, C.D., Mettler-
916 Altmann, T., Soubeyrand, E., Weber, A.P.M., Lipton, M.S., et al. (2019). Multiomics resolution
917 of molecular events during a day in the life of Chlamydomonas. Proc. Natl. Acad. Sci. U. S. A.
918 *116*, 2374–2383. https://doi.org/10.1073/pnas.1815238116.

919 Suzuki, N., Koussevitzky, S., Mittler, R., and Miller, G. (2012). ROS and redox signalling in the
920 response of plants to abiotic stress. Plant Cell Environ. *35*, 259–270.
921 https://doi.org/10.1111/j.1365-3040.2011.02336.x.

922 Urzica, E.I., Vieler, A., Hong-Hermesdorf, A., Page, M.D., Casero, D., Gallaher, S.D., Kropat, J.,
923 Pellegrini, M., Benning, C., and Merchant, S.S. (2013). Remodeling of membrane lipids in iron-
924 starved Chlamydomonas. J. Biol. Chem. *288*, 30246–30258.
925 https://doi.org/10.1074/jbc.M113.490425.

926 Vevea, J.D., Alessi Wolken, D.M., Swayne, T.C., White, A.B., and Pon, L.A. (2013). Ratiometric
927 biosensors that measure mitochondrial redox state and ATP in living yeast cells. J. Vis. Exp. 50633.
928 https://doi.org/10.3791/50633.

929 Wakao, S., and Niyogi, K.K. (2021). Chlamydomonas as a model for reactive oxygen species
930 signaling and thiol redox regulation in the green lineage. Plant Physiol. *187*, 687–698.
931 https://doi.org/10.1093/plphys/kiab355.

932 Walters, R.G., Ibrahim, D.G., Horton, P., and Kruger, N.J. (2004). A mutant of Arabidopsis
933 lacking the triose-phosphate/phosphate translocator reveals metabolic regulation of starch
934 breakdown in the light. Plant Physiol. *135*, 891–906. https://doi.org/10.1104/pp.104.040469.

935 Weber, A.P.M., Linka, M., and Bhattacharya, D. (2006). Single, ancient origin of a plastid
936 metabolite translocator family in Plantae from an endomembrane-derived ancestor. Eukaryot. Cell
937 *5*, 609–612. https://doi.org/10.1128/EC.5.3.609-612.2006.

938 Winder, C.L., Dunn, W.B., Schuler, S., Broadhurst, D., Jarvis, R., Stephens, G.M., and Goodacre,
939 R. (2008). Global metabolic profiling of *Escherichia coli* cultures: an evaluation of methods for
940 quenching and extraction of intracellular metabolites. Anal. Chem. *80*, 2939–2948.
941 https://doi.org/10.1021/ac7023409.

942 Young, J.D., Shastri, A.A., Stephanopoulos, G., and Morgan, J.A. (2011). Mapping
943 photoautotrophic metabolism with isotopically nonstationary $^{(13)}$C flux analysis. Metab. Eng. *13*,
944 656–665. https://doi.org/10.1016/j.ymben.2011.08.002.

945 Yu, E.T., Zendejas, F.J., Lane, P.D., Gaucher, S., Simmons, B.A., and Lane, T.W. (2009).
946 Triacylglycerol accumulation and profiling in the model diatoms *Thalassiosira pseudonana* and
947 *Phaeodactylum tricornutum* (Baccilariophyceae) during starvation. J. Appl. Phycol. *21*, 669–681.
948 https://doi.org/10.1007/s10811-008-9400-y.

949 Zhao, Y., Luo, L., Xu, J., Xin, P., Guo, H., Wu, J., Bai, L., Wang, G., Chu, J., Zuo, J., et al. (2018).
950 Malate transported from chloroplast to mitochondrion triggers production of ROS and PCD in
951 *Arabidopsis thaliana*. Cell Res. *28*, 448–461. https://doi.org/10.1038/s41422-018-0024-8.

952 Zhao, Y., Yu, H., Zhou, J.-M., Smith, S.M., and Li, J. (2020). Malate circulation: linking
953 chloroplast metabolism to mitochondrial ROS. Trends Plant Sci. *25*, 446–454.
954 https://doi.org/10.1016/j.tplants.2020.01.010.

955 Zirngibl, M.-E., Araguirang, G.E., Kitashova, A., Jahnke, K., Rolka, T., Kühn, C., Nägele, T., and
956 Richter, A.S. (2022). Triose phosphate export from chloroplasts and cellular sugar content regulate
957 anthocyanin biosynthesis during high light acclimation. Plant Commun 100423.
958 https://doi.org/10.1016/j.xplc.2022.100423.

959 Zones, J.M., Blaby, I.K., Merchant, S.S., and Umen, J.G. (2015). High-Resolution Profiling of a
960 Synchronized Diurnal Transcriptome from *Chlamydomonas reinhardtii* Reveals Continuous Cell
961 and Metabolic Differentiation. Plant Cell *27*, 2743–2769. https://doi.org/10.1105/tpc.15.00498.

962

963 **Legends**

964 **Fig. 1: Subcellular localization of CreTPT3 and in vitro measurements of CreTPT3 transport**
965 **activities.** (**A**) Cellular localization of CreTPT3. The construct for expression of the CreTPT3-VENUS
966 fusion protein is shown above the cell images and described in the **Materials and methods**. VENUS
967 fluorescence, green; Chlorophyll (Chl) autofluorescence, magenta. (Scale bar: 5 µm). (**B**) Expression of
968 Cre*TPT3* in yeast. Left, SDS-PAGE of proteins from total membranes isolated from yeast cells containing
969 the empty vector (lane 1) or expressing His-CreTPT3 (lane 2). Right, corresponding immunoblot blot
970 detection of recombinant His-CreTPT3 protein using anti-His antibodies. The calculated molecular mass
971 of the N-terminal His-tagged protein was 37 kDa. (**C**) The kinetics of Pi exchange by His-CreTPT3 in lipid
972 vesicles. Uptake of Pi (0.25 mM) into liposomes was measured in the presence (■) or absence (□) of Pi
973 (30 mM) loaded within the vesicles. The arithmetic mean (±SD) of three independent experiments (each
974 with three technical replicates) was plotted with respect to the time after initiating the assay. (**D**) Analyses
975 of substrate specificity of His-CreTPT3. Liposomes in which His-CreTPT3 was incorporated were
976 preloaded with various substrates (30 mM) and the initial Pi uptake rates (at 0.25 mM external concentration)
977 were determined. Relative velocities were compared to the Pi/Pi homo-exchange, which was set to 100%.
978 The data represents the arithmetic mean (±SD) of three independent experiments (each consisting of three
979 technical replicates). (**E**) Comparison of kinetic constants of CreTPT3. The Michaelis-Menten constant (K_M)
980 for Pi uptake was determined using various external Pi concentrations (0.05-5 mM). The competitive
981 inhibition constant (K_i) of Pi uptake (0.25 mM) was measured with increasing competitor concentrations
982 (0.05-5 mM). Liposomes were preloaded with 30 mM Pi as the counter-exchange substrate. The data
983 represent the arithmetic mean +/- SE of three independent experiments. ND, no competitive inhibitory
984 constant could be measured under the given experimental conditions. DHAP, dihydroxyacetone phosphate;
985 3-PGA, 3-phosphoglycerate; PEP, phosphoenolpyruvate; Glc6P, glucose 6-P; Glc1P, glucose 1-P; Fru6P,
986 fructose 6-P; Gal1P, galactose 1-P.

987 **Fig. 2: Growth characterization of *tpt3* mutants and complemented strains.** (**A-B**) Cre*TPT3* and the
988 positions edited using CRISPR-Cas9. Molecular map of Cre*TPT3* gene and positions of the Cas9 targeted
989 sites (**A**) Edited sites are located in exons 1 and 7; *t3ko1* has the marker gene inserted in exon 1 and *t3ko2*
990 and *t3ko3* has the marker gene inserted in exon 7. (**B**) Immunoblot (left panel) of the stained protein profiles
991 (right panel) for wild type, *t3ko1*, *t3ko2*, *t3ko3* and the complemented strains (*C_T3KO1*, *C_T3KO2* and
992 *C_T3KO3*, respectively). (**C**) Growth of WT, *t3ko1*, *t3ko2*, *t3ko3* and the complemented strains (*C_T3KO1*,
993 *C_T3KO2*, and *C_T3KO3*, respectively), at various dilutions (see below) on agar plates incubated under
994 LL and ML for 4 d. (**D**) Growth of the various strains (indicated) in liquid medium under LL (left panel)
995 and ML (right panel). (**E**) Transition of the strains from LL to ML (upper panel) or to high light (HL, 450
996 µmol photons m^{-2} s^{-1}) (lower panel) for the times indicated. (**F**) Cell growth (number) and chlorophyll
997 content of cultures at various times after shifting from LL to ML for up to 48 h. In (**C**) the cells were spotted
998 on agar plates containing TAP or TP medium and maintained under continuous LL or ML conditions. The
999 dilution series used was 1.5, 0.75, 0.375 µg/mL chlorophyll (left to right). For growth in liquid medium,
1000 the cells were cultured in TP medium to an initial OD_{750nm} 0.02 in air and under continuous LL before
1001 initiating the various growth analyses in LL, ML or HL. Each curve represents the arithmetic mean (±SD)
1002 of three independent experiments.
1003

1004 **Fig. 3: Changes in storage carbon and metabolite levels in WT and *t3ko2* after transitioning cells**
1005 **from growth in LL to ML.** (**A**) Starch content in indicated strains following 0, 6, and 24 h of ML exposure.
1006 (**B**) Lugol staining of starch in WT and *t3ko2* after 48 h of ML. (**C**) TAG (TAG: triacylglycerol) content in
1007 the indicated strains following 0, 6, and 24 h of ML exposure. (**D**) Nile Red staining of TAG in WT and
1008 *t3ko2* following 48 h of ML exposure. (**E**) Time course of metabolite accumulation at 0 h (LL), 45 min and
1009 6 h following ML exposure. (**F**) Select metabolic pathways in Chlamydomonas adapted from (Johnson and
1010 Alric, 2013). (**G**) Bar graph representation of fold-change for metabolites shown in (**E**); calculated by
1011 dividing the pool size in *t3ko2* by that of WT at the respective light levels. A fold change of 1 (no change)
1012 is indicated with a dashed line. Each data point shows the mean and standard error; the data represents three
1013 biological replicates for each metabolite. An asterisk indicates statistically significant differences compared
1014 to WT (* P<0.05, ** P<0.01, *** P<0.001). Abbreviations: G6P, glucose-6-P; FBP, fructose bisphosphate;
1015 DHAP, dihydroxyacetone phosphate; 3-PGA, 3-phosphoglycerate; PEP, phosphoenolpyruvate; PYR,
1016 pyruvate; CIT, citrate; SUCC, succinate; FUM, fumarate; MAL, malate; E4P, Erythrose 4-P; R5P, Ribose
1017 5-P; RU5P/X5P, ribulose 5-P/xylulose-5-P; OMT, 2-oxoglutarate/malate transporter.

1018 **Fig. 4: Photosynthetic activities followed LL to ML or HL transitions.** (**A**) O_2 evolution of LL (left) and
1019 ML (right)-acclimated cells for the indicated strains. (**B**) Fv/Fm of WT, *t3ko2* and the rescued strain
1020 (*C_T3KO2*) following 0 (LL), 6 and 24 h in ML. (**C**) 1-qL values of LL (left panel) and ML (right panel)
1021 acclimated cells exposed to increasing actinic light intensities. (**D**) Kinetics of 1-qL of LL-acclimated cells
1022 after illumination at HL (400-450 µmol photons m^{-2} s^{-1}) actinic light for the times indicated on the x-axis.
1023 (**E**) P700 oxidation and reduction kinetics in LL-grown cells and after 6 and 24 h in ML. (**F**) Kinetics of
1024 P700 oxidation upon dark-to-light transition**.** P700 measurements were made in the presence of DCMU and
1025 hydroxylamine, as indicated in the **Materials and methods**. Absorbance differences were monitored at 705
1026 nm during continuous illumination with 150 µmol photons·m^{-2} s^{-1} for 5 sec (white box above), followed by
1027 a saturating light pulse at 1,500 µmol photons·m^{-2} s^{-1} (arrow) and a 5 sec dark incubation (black box). For
1028 panel E, kinetics was normalized by setting maximum oxidation (after light pulse) of WT to 100% and for
1029 panel F, by setting maximum oxidation (after light pulse) of individual strain to 100%. The data from all
1030 panels represent the arithmetic mean (±SD) of three independent experiments. For panel **B**, the asterisks
1031 represent significant differences determined by ANOVA tests., ****P < 0.0001.

1032 **Fig. 5: Measurement of intracellular ROS in *t3ko2* and WT upon transition from LL to ML.** (**A**) ROS
1033 levels were evaluated by CM-H2DCFDA fluorescence of WT and the *t3ko2* mutant in LL and following
1034 exposure to ML for 48 h. (**B**) Quantitation of data in **A**. roGFP2 protein was targeted to the chloroplast
1035 stroma (**C**, upper panel) and mitochondrion (**C**, lower panel). BF: bright field; roGFP2 fluorescence: green;
1036 Chlorophyll (Chl) autofluorescence: red. (**D-E**) Monitoring redox levels in stroma (**D**) and mitochondrion
1037 (**E**) after exposure of WT and the *t3ko2* mutant for 1.5 and 6.0 h of ML. Shown are mean values from three
1038 independent experiments, error bars represent standard deviation. For panel **B** and **D**, the asterisks represent
1039 significant differences determined by ANOVA tests., **P < 0.005, ***P < 0.001.

1040

1041 **Fig. 6: Real-time monitor of H_2O_2 distribution in *t3ko2* and WT upon transition from LL to HL.** (**A**)
1042 The hypersensitive H_2O_2 sensor (roGFP2-Tsa2ΔCR) protein was targeted to the chloroplast stroma (St),
1043 cytosol (Cyto), mitochondrion (Mito) and nucleus (Nu). Shown are GFP fluorescence, chlorophyll
1044 autofluorescence (Chl) and the two signals merged (scale bar: 5 µm). WT and *t3ko2* transformant cells,
1045 accumulating roGFP2-Tsa2ΔCR in the stroma (**B**), cytosol (**C**), mitochondrial matrix (**D**), and nucleus (**E**),
1046 were acclimated to LL in TP and then were transferred either to HL (450 µmol photons m^{-2} s^{-1}, solid line)
1047 or to very LL (10 µmol photons m^{-2} s^{-1}, dotted line). The oxidation state of the sensor was trapped by the
1048 addition of NEM and roGFP2 fluorescence was measured in a plate reader as previously described
1049 (Niemeyer et al., 2021). Shown are mean values from three independent experiments with the error bars
1050 representing the standard deviation.

1051 **Fig. 7: Impact of eliminating Chlamydomonas TPT3 on the chloroplast metabolic landscape. i.**
1052 reduced triose-P export leads to accumulation of the sugar-P in CBBC and glycolysis pathways (e.g. triose-
1053 P, hexose-P, marked in orange), and an elevated ratio of 3-PGA/Pi (which can allosterically activate
1054 AGPase activity) would begin to stimulate production of storage carbon; **ii.** CBBC activity diminishes as a
1055 consequence of the hyper-accumulation of the precursors along with the fixation of CO_2, leading to
1056 elevation of reductant (NADPH) and energy (ATP) within the chloroplast; the elevated NADPH:$NADP^+$
1057 and ATP:ADP ratios, elicit strong feedback on PET causing hyper-reduction of electron carriers (eg: over
1058 reduced PQ pool and highly reduced PSI) that slows electron flow across the cytochrome b_6f complex; **iii.**
1059 the highly reduced PET system and the elevated NADPH can actively reduce FDX/TRX and the NTRC
1060 systems, respectively; reduced TRX and/or NTRC can activate the AGPase (above the activity elicited by
1061 an increase in the 3-PGA/Pi ratio), leading to additional starch accumulation; **iv.** hyper-reduction of PET
1062 can also lead to stromal ROS accumulation, that can act as a signal that controls expression of chloroplast
1063 and nuclear genes; ROS also cause damage to both PSII and I and leads to neutral lipid (TAG:
1064 triacylglycerol) accumulation as a consequence of activation of diacylglycerol acyltransferases (DGAT)
1065 and phospholipid diacylglycerol acyltransferase (PDAT). Many of these metabolic/acclimatory processes
1066 both overlap and are interconnected. Under conditions of extended exposure to ML, the damage in
1067 Chlamydomonas *tpt3* mutants can accumulate and lead to cell death; cell death occurs rapidly in high light.
1068

1069 **Figures and Tables**

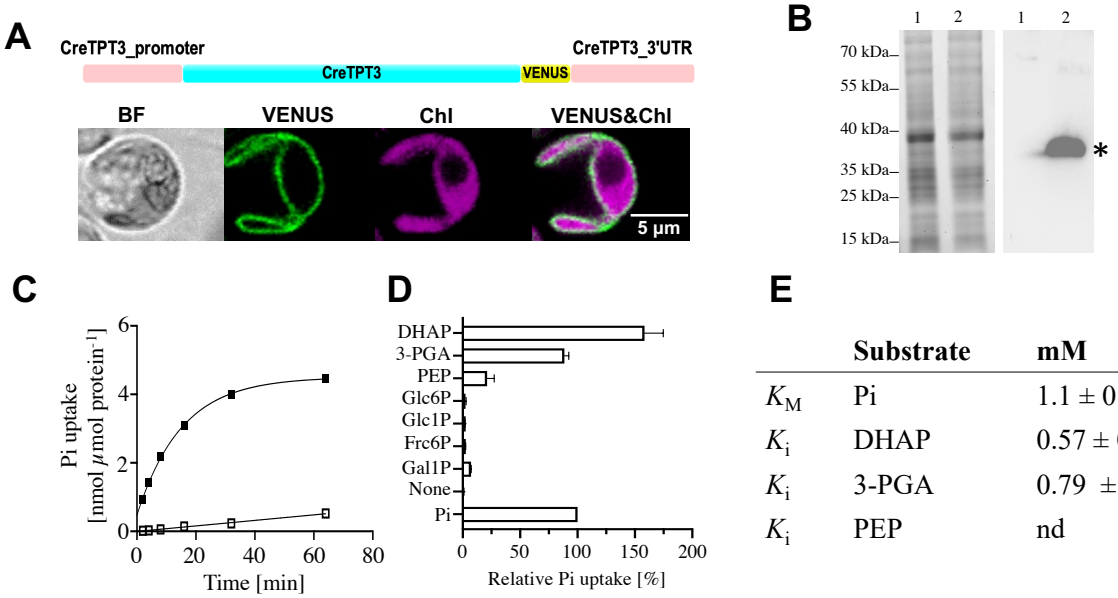

E

	Substrate	mM
K_M	Pi	1.1 ± 0.2
K_i	DHAP	0.57 ± 0.013
K_i	3-PGA	0.79 ± 0.122
K_i	PEP	nd

1070

1071 **Fig. 1: Subcellular localization of CreTPT3 and in vitro measurements of CreTPT3 transport**
1072 **activities.** (**A**) Cellular localization of CreTPT3. The construct for expression of the CreTPT3-VENUS
1073 fusion protein is shown above the cell images and described in the **Materials and methods**. VENUS
1074 fluorescence, green; Chlorophyll (Chl) autofluorescence, magenta. (Scale bar: 5 µm). (**B**) Expression of
1075 Cre*TPT3* in yeast. Left, SDS-PAGE of proteins from total membranes isolated from yeast cells containing
1076 the empty vector (lane 1) or expressing His-CreTPT3 (lane 2). Right, corresponding immunoblot blot
1077 detection of recombinant His-CreTPT3 protein using anti-His antibodies. The calculated molecular mass
1078 of the N-terminal His-tagged protein was 37 kDa. (**C**) The kinetics of Pi exchange by His-CreTPT3 in lipid
1079 vesicles. Uptake of Pi (0.25 mM) into liposomes was measured in the presence (■) or absence (□) of Pi
1080 (30 mM) loaded within the vesicles. The arithmetic mean (±SD) of three independent experiments (each
1081 with three technical replicates) was plotted with respect to the time after initiating the assay. (**D**) Analyses
1082 of substrate specificity of His-CreTPT3. Liposomes in which His-CreTPT3 was incorporated were
1083 preloaded with various substrates (30 mM) and the initial Pi uptake rates (at 0.25 mM external concentration)
1084 were determined. Relative velocities were compared to the Pi/Pi homo-exchange, which was set to 100%.
1085 The data represents the arithmetic mean (±SD) of three independent experiments (each consisting of three
1086 technical replicates). (**E**) Comparison of kinetic constants of CreTPT3. The Michaelis-Menten constant (K_M)
1087 for Pi uptake was determined using various external Pi concentrations (0.05-5 mM). The competitive
1088 inhibition constant (K_i) of Pi uptake (0.25 mM) was measured with increasing competitor concentrations
1089 (0.05-5 mM). Liposomes were preloaded with 30 mM Pi as the counter-exchange substrate. The data
1090 represent the arithmetic mean +/- SE of three independent experiments. ND, no competitive inhibitory
1091 constant could be measured under the given experimental conditions. DHAP, dihydroxyacetone phosphate;
1092 3-PGA, 3-phosphoglycerate; PEP, phosphoenolpyruvate; Glc6P, glucose 6-P; Glc1P, glucose 1-P; Fru6P,
1093 fructose 6-P; Gal1P, galactose 1-P.

1094

1095

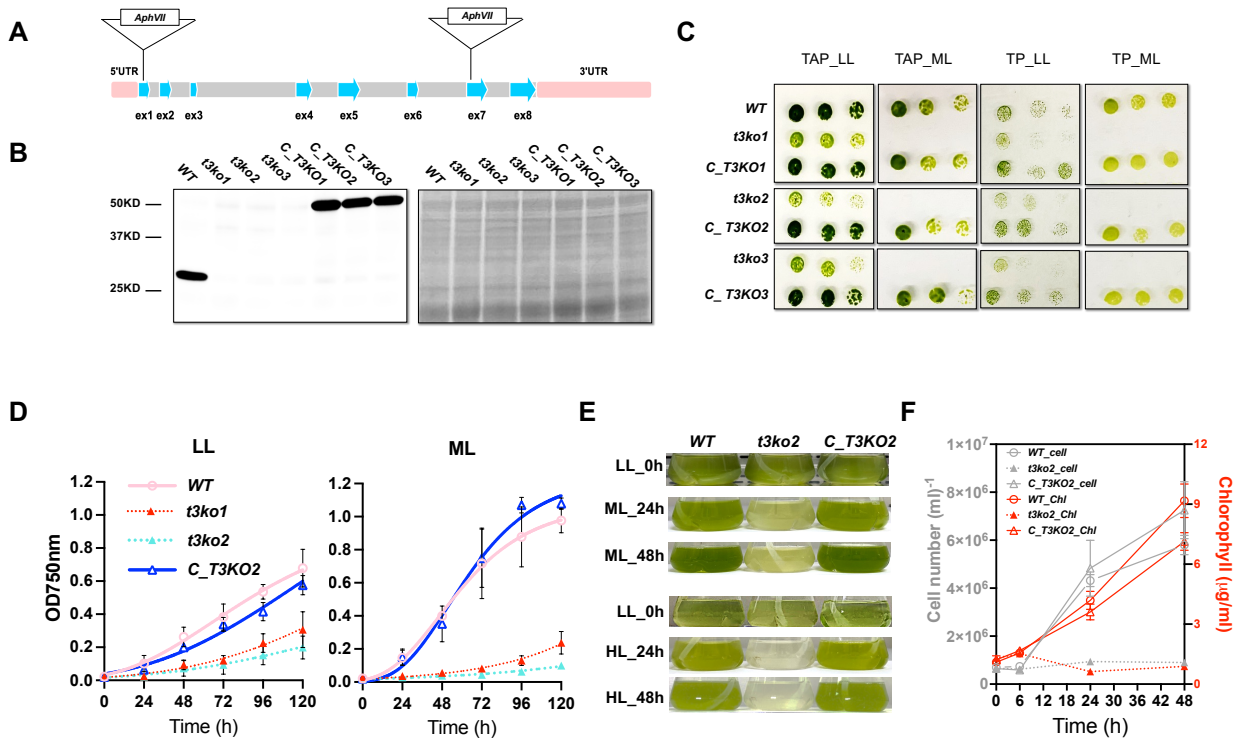

Fig. 2: Growth characterization of *tpt3* mutants and complemented strains. (**A-B**) Cre*TPT3* and the positions edited using CRISPR-Cas9. Molecular map of Cre*TPT3* gene and positions of the Cas9 targeted sites (**A**) Edited sites are located in exons 1 and 7; *t3ko1* has the marker gene inserted in exon 1 and *t3ko2* and *t3ko3* has the marker gene inserted in exon 7. (**B**) Immunoblot (left panel) of the stained protein profiles (right panel) for wild type, *t3ko1*, *t3ko2*, *t3ko3* and the complemented strains (*C_T3KO1*, *C_T3KO2* and *C_T3KO3*, respectively). (**C**) Growth of WT, *t3ko1*, *t3ko2*, *t3ko3* and the complemented strains (*C_T3KO1*, *C_T3KO2*, and *C_T3KO3*, respectively), at various dilutions (see below) on agar plates incubated under LL and ML for 4 d. (**D**) Growth of the various strains (indicated) in liquid medium under LL (left panel) and ML (right panel). (**E**) Transition of the strains from LL to ML (upper panel) or to high light (HL, 450 µmol photons m^{-2} s^{-1}) (lower panel) for the times indicated. (**F**) Cell growth (number) and chlorophyll content of cultures at various times after shifting from LL to ML for up to 48 h. In (**C**) the cells were spotted on agar plates containing TAP or TP medium and maintained under continuous LL or ML conditions. The dilution series used was 1.5, 0.75, 0.375 µg/mL chlorophyll (left to right). For growth in liquid medium, the cells were cultured in TP medium to an initial OD_{750nm} 0.02 in air and under continuous LL before initiating the various growth analyses in LL, ML or HL. Each curve represents the arithmetic mean (±SD) of three independent experiments.

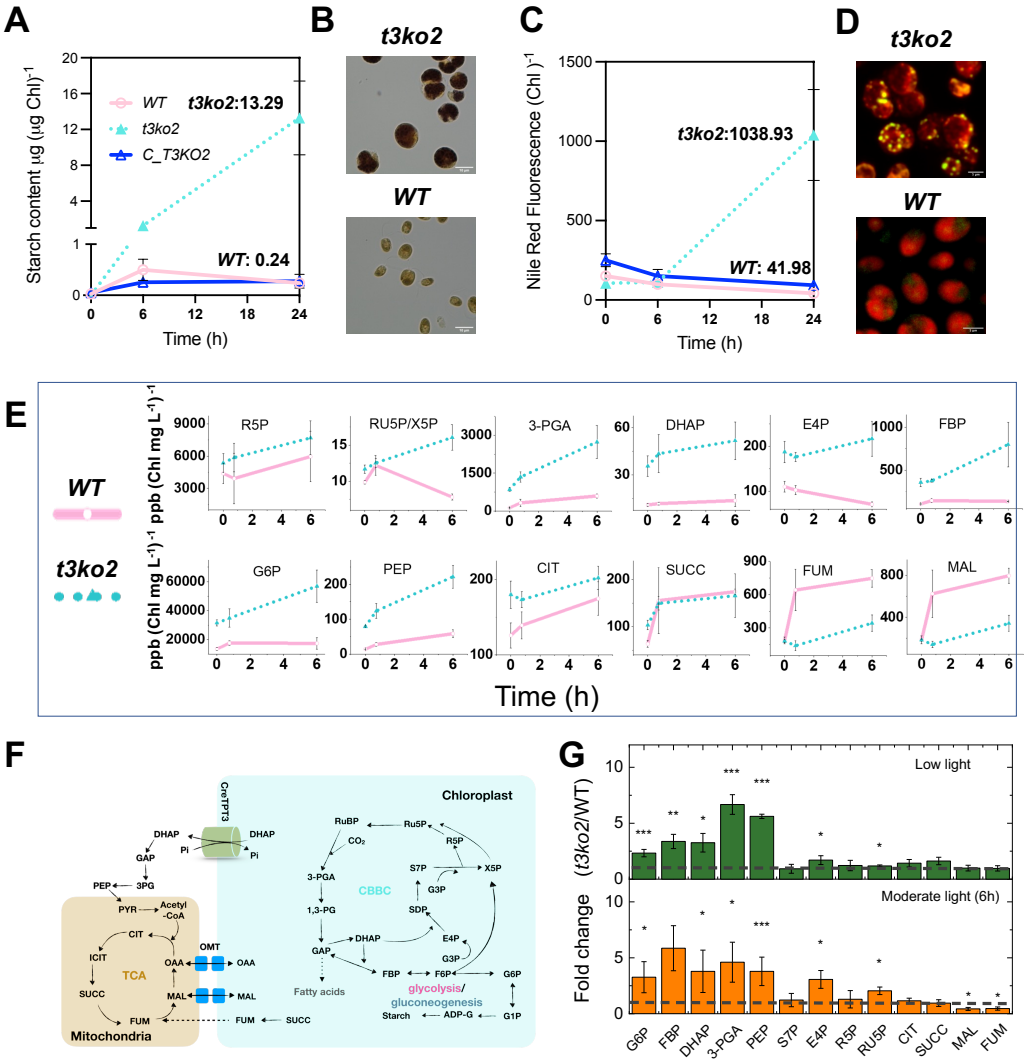

Fig. 3: Changes in storage carbon and metabolite levels in WT and *t3ko2* after transitioning cells from growth in LL to ML. (**A**) Starch content in indicated strains following 0, 6, and 24 h of ML exposure. (**B**) Lugol staining of starch in WT and *t3ko2* after 48 h of ML. (**C**) TAG (TAG: triacylglycerol) content in the indicated strains following 0, 6, and 24 h of ML exposure. (**D**) Nile Red staining of TAG in WT and *t3ko2* following 48 h of ML exposure. (**E**) Time course of metabolite accumulation at 0 h (LL), 45 min and 6 h following ML exposure. (**F**) Select metabolic pathways in Chlamydomonas adapted from (Johnson and Alric, 2013). (**G**) Bar graph representation of fold-change for metabolites shown in (**E**); calculated by dividing the pool size in *t3ko2* by that of WT at the respective light levels. A fold change of 1 (no change) is indicated with a dashed line. Each data point shows the mean and standard error; the data represents three biological replicates for each metabolite. An asterisk indicates statistically significant differences compared to WT (* P<0.05, ** P<0.01, *** P<0.001). Abbreviations: G6P, glucose-6-P; FBP, fructose bisphosphate; DHAP, dihydroxyacetone phosphate; 3-PGA, 3-phosphoglycerate; PEP, phosphoenolpyruvate; PYR, pyruvate; CIT, citrate; SUCC, succinate; FUM, fumarate; MAL, malate; E4P, Erythrose 4-P; R5P, Ribose 5-P; RU5P/X5P, ribulose 5-P/xylulose-5-P; OMT, 2-oxoglutarate/malate transporter.

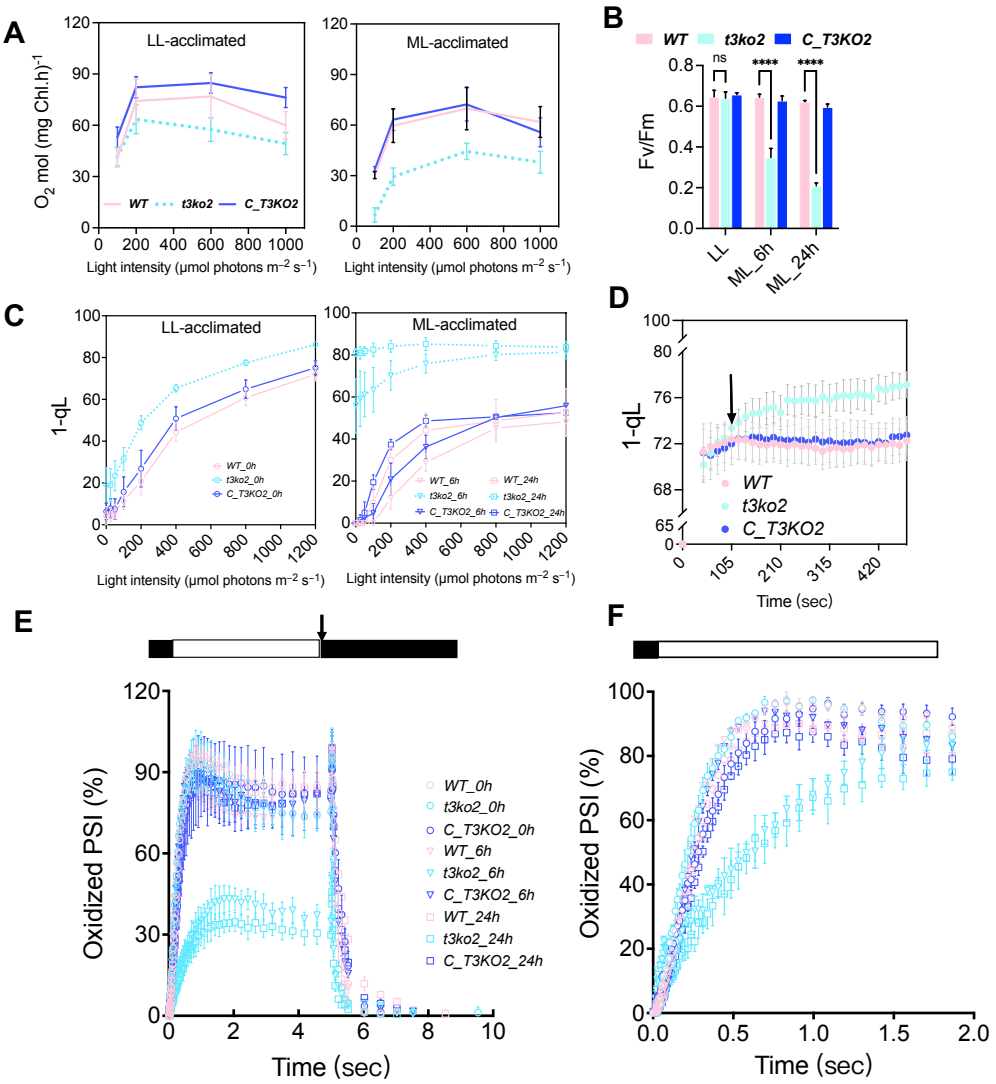

Fig. 4: Photosynthetic activities followed LL to ML or HL transitions. (**A**) O_2 evolution of LL (left) and ML (right)-acclimated cells for the indicated strains. (**B**) Fv/Fm of WT, *t3ko2* and the rescued strain (*C_T3KO2*) following 0 (LL), 6 and 24 h in ML. (**C**) 1-qL values of LL (left panel) and ML (right panel) acclimated cells exposed to increasing actinic light intensities. (**D**) Kinetics of 1-qL of LL-acclimated cells after illumination at HL (400-450 µmol photons m^{-2} s^{-1}) actinic light for the times indicated on the x-axis. (**E**) P700 oxidation and reduction kinetics in LL-grown cells and after 6 and 24 h in ML. (**F**) Kinetics of P700 oxidation upon dark-to-light transition**.** P700 measurements were made in the presence of DCMU and hydroxylamine, as indicated in the **Materials and methods**. Absorbance differences were monitored at 705 nm during continuous illumination with 150 µmol photons·m^{-2} s^{-1} for 5 sec (white box above), followed by a saturating light pulse at 1,500 µmol photons·m^{-2} s^{-1} (arrow) and a 5 sec dark incubation (black box). For panel E, kinetics was normalized by setting maximum oxidation (after light pulse) of WT to 100% and for panel F, by setting maximum oxidation (after light pulse) of individual strain to 100%. The data from all panels represent the arithmetic mean (±SD) of three independent experiments. For panel **B**, the asterisks represent significant differences determined by ANOVA tests., ****P < 0.0001.

1146

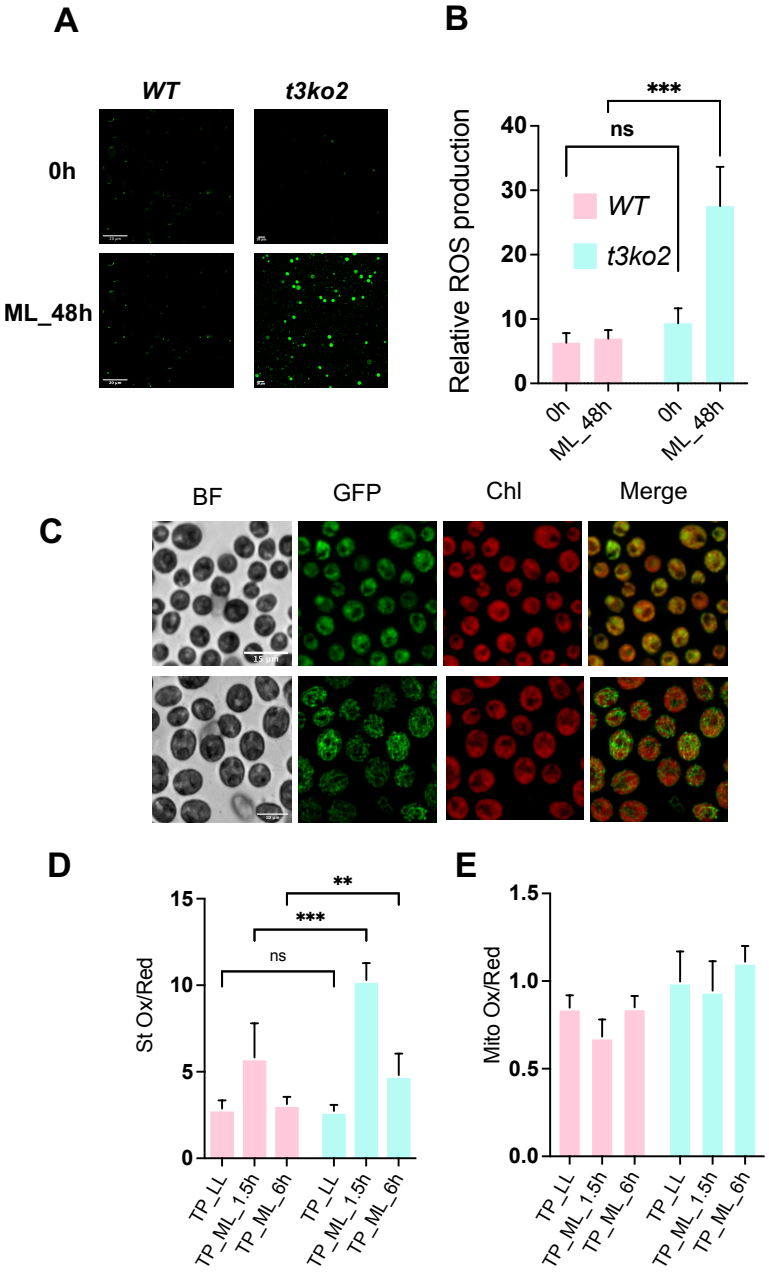

1147

1148 **Fig. 5: Measurement of intracellular ROS in *t3ko2* and WT upon transition from LL to ML.** (**A**) ROS
1149 levels were evaluated by CM-H2DCFDA fluorescence of WT and the *t3ko2* mutant in LL and following
1150 exposure to ML for 48 h. (**B**) Quantitation of data in **A**. roGFP2 protein was targeted to the chloroplast
1151 stroma (**C**, upper panel) and mitochondrion (**C**, lower panel). BF: bright field; roGFP2 fluorescence: green;
1152 Chlorophyll (Chl) autofluorescence: red. (**D-E**) Monitoring redox levels in stroma (**D**) and mitochondrion
1153 (**E**) after exposure of WT and the *t3ko2* mutant for 1.5 and 6.0 h of ML. Shown are mean values from three
1154 independent experiments, error bars represent standard deviation. For panel **B** and **D**, the asterisks represent
1155 significant differences determined by ANOVA tests., **P < 0.005, ***P < 0.001.

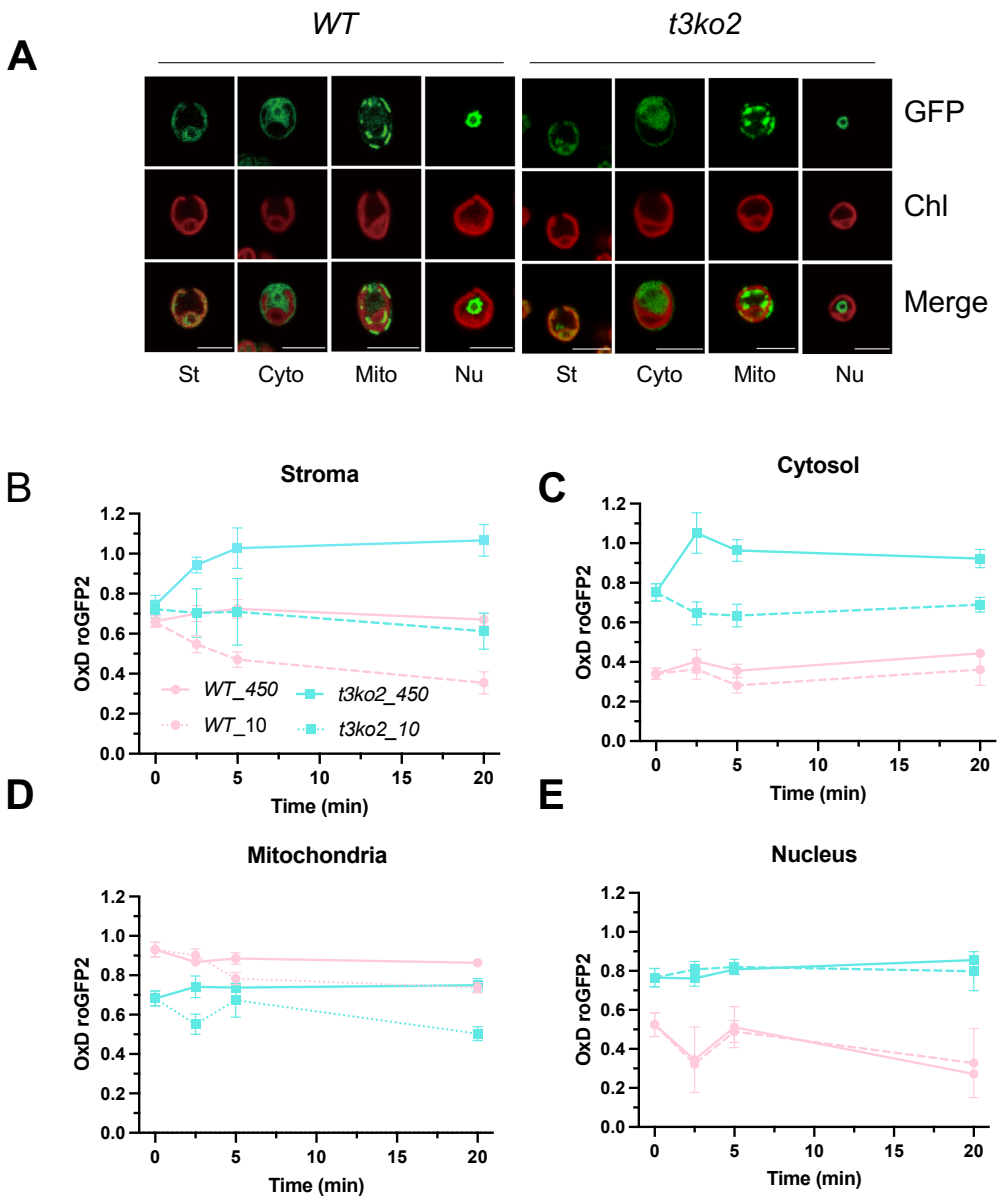

Fig. 6: Real-time monitor of H_2O_2 compartmentalized distribution in *t3ko2* and WT upon transition from LL to HL. (**A**) The hypersensitive H_2O_2 sensor (roGFP2-Tsa2ΔCR) protein was targeted to the chloroplast stroma (St), cytosol (Cyto), mitochondrion (Mito) and nucleus (Nu). Shown are GFP fluorescence, chlorophyll autofluorescence (Chl) and the two signals merged (scale bar: 5 µm). WT and *t3ko2* transformant cells, accumulating roGFP2-Tsa2ΔCR in the stroma (**B**), cytosol (**C**), mitochondrial matrix (**D**), and nucleus (**E**), were acclimated to LL in TP and then were transferred either to HL (450 µmol photons m^{-2} s^{-1}, solid line) or to very LL (10 µmol photons m^{-2} s^{-1}, dotted line). The oxidation state of the sensor was trapped by the addition of NEM and roGFP2 fluorescence was measured in a plate reader as previously described (Niemeyer et al., 2021). Shown are mean values from three independent experiments with the error bars representing the standard deviation.

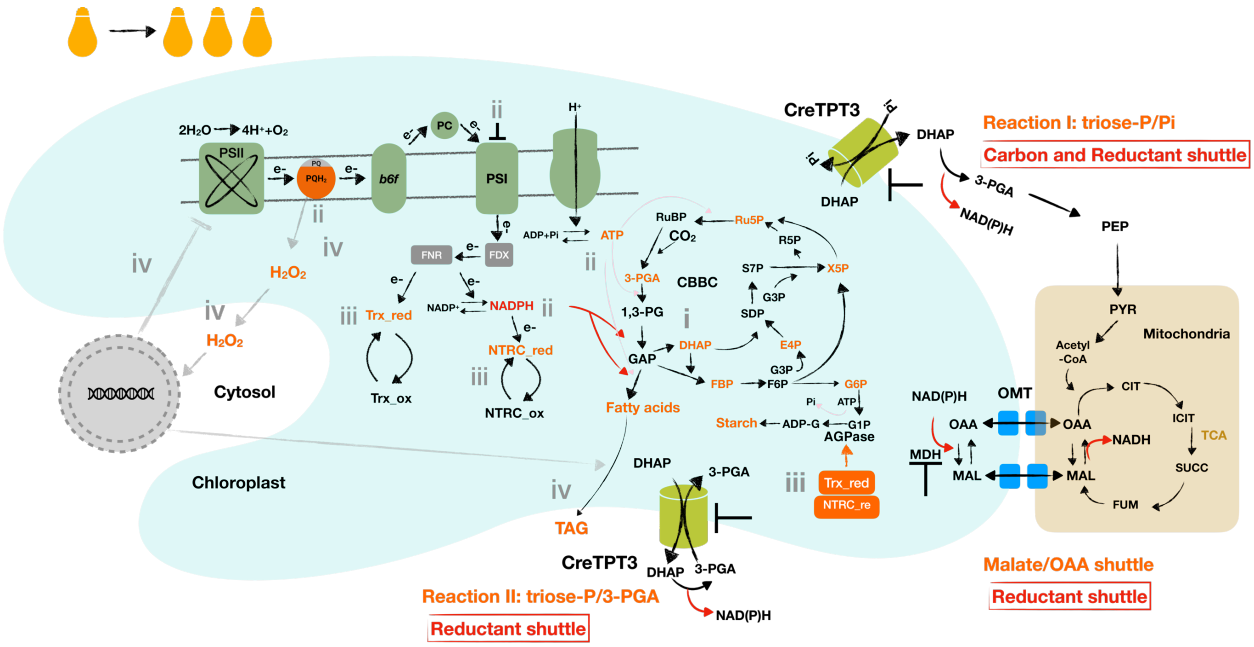

Fig. 7: Impact of eliminating Chlamydomonas TPT3 on the chloroplast metabolic landscape. i. reduced triose-P export leads to accumulation of the sugar-P in CBBC and glycolysis pathways (e.g. triose-P, hexose-P, marked in orange), and an elevated ratio of 3-PGA/Pi (which can allosterically activate AGPase activity) would begin to stimulate production of storage carbon; **ii.** CBBC activity diminishes as a consequence of the hyper-accumulation of the precursors along with the fixation of CO_2, leading to elevation of reductant (NADPH) and energy (ATP) within the chloroplast; the elevated NADPH:$NADP^+$ and ATP:ADP ratios, elicit strong feedback on PET causing hyper-reduction of electron carriers (eg: over reduced PQ pool and highly reduced PSI) that slows electron flow across the cytochrome *b₆f* complex; **iii.** the highly reduced PET system and the elevated NADPH can actively reduce FDX/TRX and the NTRC systems, respectively; reduced TRX and/or NTRC can activate the AGPase (above the activity elicited by an increase in the 3-PGA/Pi ratio), leading to additional starch accumulation; **iv.** hyper-reduction of PET can also lead to stromal ROS accumulation, that can act as a signal that controls expression of chloroplast and nuclear genes; ROS also cause damage to both PSII and I and leads to neutral lipid accumulation as a consequence of activation of diacylglycerol acyltransferases (DGAT) and phospholipid diacylglycerol acyltransferase (PDAT). Many of these metabolic/acclimatory processes both overlap and are interconnected. Under conditions of extended exposure to ML, the damage in Chlamydomonas *tpt3* mutants can accumulate and lead to cell death; cell death occurs rapidly in high light.

1187 **Supplementary Materials**

1188 **Materials and methods**

1189 **Expression of CreTPT3 in yeast**

1190 The DNA sequence encoding the mature CreTPT3 protein was codon-optimized for expression in
1191 *Saccharomyces cerevisiae* (GeneART, ThermoFisher Scientific). This coding sequence was inserted in
1192 frame with an N-terminal His tag into the yeast vector pYES-NTa (ThermoFisher Scientific) using Gibson
1193 cloning (NEB). Briefly, pYES-NTa was linearized with BamHI and the CreTPT3 cDNA amplified with the
1194 primer pair fwd:5'- gacgataaggtacctagcGCTTCTGCTGCTGATGCTC-3' and rev:5'-
1195 agaattccaccacactgTTAAGCGGCAGCTGGAGAAG-3'. This cDNA was ligated into the linearized pYES-
1196 NTa vector, which was then transformed into the yeast strain INVSc1 (MATa, his3D1, leu2, trp1-289, ura3-
1197 52 / MATa, his3D1, leu2, trp1-289, and ura3-52, Thermo Fisher Scientific) using the lithium-acetate/PEG
1198 method (Gietz and Schiestl, 2007). Transformed yeast cells were selected on synthetic complete medium
1199 containing 2% (w/v) glucose with the uracil auxotrophic marker. Galactose-inducible expression of His-
1200 CreTPT3 in yeast was performed as described in (Linka et al., 2008). The presence of the His-tagged fusion
1201 protein was verified by standard SDS-PAGE and immunoblot analysis using an anti-His-antibody
1202 conjugated with horseradish peroxidase (Miltenyi Biotech).

1203 **Transport activity assays**

1204 The Km for Pi was determined by measuring the initial velocity at each of six external Pi concentrations
1205 between 0.05 and 5 mM. To obtain competitive inhibition constants (Ki), the uptake of 0.25 mM Pi into
1206 liposomes containing 30 mM Pi was measured over a 4 min period in the presence of increasing external
1207 competitor concentrations (0.05 - 5 mM). Three biological replicates were performed for all described
1208 experiments. GraphPad Prism software version 9.3.0 was used for non-linear regression analyses of the
1209 kinetic data.

1210 **Vector construction**

1211 This plasmid was linearized with HpaI (NEB). Primers: g*TPT3*_pRam118_f and g*TPT3*_pRam118_r
1212 (**Supplementary Table 1**) were used to amplify Cre*TPT3* genomic DNA containing an overlap with the
1213 linearized pRam118_VENUS vector. For generating the plasmid pRam118-CreTPT3&VENUS, genomic
1214 DNA of Cre*TPT3* was assembled with pRam118_VENUS plasmid using Gibson assembly(Gibson et al.,
1215 2009). A 1,000 bp sequence upstream of Cre*TPT3* and containing the promoter region of the gene was
1216 amplified using the primers TPT3pro1000_f and TPT3pro1000_r (**Supplementary Table 1**). The 3' UTR
1217 of Cre*TPT3* was amplified using TPT_3UTR_f and TPT3_3UTR_r (**Supplementary Table 1**). The *PSAD*
1218 promoter and the *RBCS2* 3'UTR of pRam118-CreTPT3&VENUS were replaced by the amplified
1219 fragments of the 1,000 bp upstream region and the 3' UTR of Cre*TPT3*, respectively. This final vector,
1220 designated pRam118_CreTPT3, contains the original Cre*TPT3* promoter (driving expression of Cre*TPT3*),
1221 the genomic DNA sequence of Cre*TPT3*, VENUS and the Cre*TPT3* 3' UTR plus the *AphVII* cassette. The
1222 Chlamydomonas *tpt3* mutant was transformed by electroporation with a total amount of 2 µg (~500 ng/µL)
1223 of pRam118_CreTPT3 that was linearized with AseI.

1224

1225

1226 **CRISPR-Cas9 mediated mutagenesis**

1227 Prior to electroporation, Cas9 (IDT) and sgRNAs were incubated together at 37 °C for 30 min.
1228 Approximately 500 ng PCR product of the *AphVII* cassette, which confers resistance to hygromycin, was
1229 added to the RNP (ribonucleoprotein) mixture. 250 µl aliquots were electroporated using Super
1230 Electroporator NEPA21 type II (NEPA GENE). After 16 h of recovery in very low light (10-15 µmol
1231 photons m^{-2} s^{-1}), cells were plated onto solid TAP medium containing 10 µg/mL hygromycin. Sense or
1232 antisense-oriented knock-ins of *AphVII* were determined by amplification using primer pairs with one
1233 primer annealing to the genomic sequence and the other to the inserted sequence (**Supplementary Table**
1234 **1**). The amplified fragments were sequenced to verify the insertion sites (ELIM BIOPHARM, Hayward,
1235 USA).

1236 **ROS measurements and roGFP2 imaging analysis**

1237 Briefly, after various treatment (e.g. 48 h in ML), 10 million Chlamydomonas cells were pelleted and
1238 washed once with 1×PBS. The cells were then resuspended in 1×PBS containing 8 µM CM-H2DCFDA
1239 and incubated at room temperature in the dark for 30 min. Following this incubation, the cells were washed
1240 three times with 1×PBS buffer, the fluorescent signals were either visualized using TCS SP8 confocal laser-
1241 scanning microscope (Leica) or quantified with a microplate reader (Infinite M1000; TECAN). Excitation
1242 and emission settings for the microscope were: 488 nm/510-530 nm HyD SMD hybrid detector for reactive
1243 oxygen species (ROS), and 488 nm/650-700 nm-HyD SMD hybrid detector for chlorophyll
1244 autofluorescence. Excitation and emission settings for the plate reader were as follows: ROS excitation
1245 488/5 nm and emission 530/12 nm; chlorophyll excitation 514/5 nm and emission 690/5 nm.

1246 **Starch analysis**

1247 In brief, cells were collected by centrifugation and pigments extracted with methanol. Dried pellets were
1248 resuspended in water and heated at 100°C to break the cells and release the starch. After cooling,
1249 amyloglucosidase and α-amylase (2.25 U/mL) were used to hydrolyze the starch and the products of
1250 hydrolysis were quantified using a Glucose Colorimetric Detection Kit (Thermo Fisher).

1251 **Photosynthesis-Irradiance curve**

1252 The YSI 5331A electrodes (Yellow Springs Instruments) were polarized at −0.8 V. The cultures used for
1253 the assays were concentrated to 2.5-5 µg mL^{-1} chlorophyll, supplemented with 15 µL of 0.5 M sodium
1254 bicarbonate in water and then purged with 1% CO_2/99% He. Using a gas tight syringe, the sample was
1255 transferred into the reaction chamber that was also purged with 1% CO_2/99% He. The rate of change in O_2
1256 levels was measured sequentially at the light intensities 100, 200, 600, 1000 µmol photons m^{-2} s^{-1}
1257 (photosynthetic active radiation, PAR); each intensity was maintained for 3-5 min followed by a 3-min
1258 intervening dark period, and then the light level was raised to the next higher intensity (stepped change)
1259 until the full range of intensities was tested. At 1,000 µmol photons m^{-2} s^{-1}, the light was held for 10 min
1260 followed by an 8-min dark period. Before the measurement of each experimental series, the electrodes were
1261 calibrated with air (~21% O_2) and 1% CO_2/99% He mixture (0% O_2). The initial slope of the response was
1262 used to determine the O_2 evolution rate.
1263

1264 **Extraction of samples for LC-MS/MS**

1265 The quenching solution, filtered saline (9 g/L NaCl), was prechilled to 4ºC in a refrigerator. 30 mL of the
1266 quenching solution was transferred to a 50 mL conical tube kept in an ice bath mixed with salt to depress
1267 the temperature to between -3ºC and -1ºC. 15 mL of the culture was rapidly plunged into the 30 mL of the
1268 quenching solution and the samples were centrifuged at 4,000 rpm for 10 min at 4ºC. Cell pellets were
1269 washed with fresh prechilled saline solution and centrifuged again at 4,000 rpm for 10 min in a 2 mL
1270 centrifuge tube. For each replicate, 45 mL of the culture was sampled and the cell pellets were pooled.
1271 Washed pellets were frozen at -80ºC until extraction. Metabolite extraction and further analysis were
1272 modified from(Young et al., 2011). To each cell pellet, 500 µL methanol was added along with the internal
1273 standards ribitol and PIPES to a final concentration of 2 µM each. Samples were then vortexed for 30 sec,
1274 frozen in liquid nitrogen as described in(Winder et al., 2008), and allowed to thaw at 0°C. This vortex-
1275 freeze-thaw cycle was repeated twice more before the samples were centrifuged at 10,000 x g at 1°C for 5
1276 min. The supernatant was collected, and the remaining pellets were extracted twice more with 500 µL of a
1277 50:50 mixture of methanol and water, with 3 vortex-freeze-thaw cycles done for each extraction.
1278 Supernatants from each extraction procedure were pooled and dried on a Thermo Fisher SpeedVac
1279 Concentrator. Dried extracts were then resuspended in 500 µL water and cleaned to remove any residual
1280 large cell debris by filtration, first through a 0.22 µm pore size Spin-X centrifugal tube filter, followed by
1281 10 K molecular mass cutoff filters, followed finally by 3 K molecular mass cutoff filters. After each
1282 filtration step, filters were rinsed with 50 µL water, which was added to the total sample volume for
1283 subsequent steps. Filtered extracts were dried again and resuspended in 200 µL water for LC-MS/MS
1284 analysis.

1285 **Protein extraction and immunoblot analysis**

1286 Affinity-purified polyclonal antibodies to CreTPT3 were custom-made by GenScript. The antigen sequence
1287 used for antibody generation was KSWSFGRPVTKQEF. Chlamydomonas cells were grown in liquid
1288 cultures to 2–5 x10^6 cells ml^{-1} and collected by centrifugation (1459 x g, 5 min). Cells were resuspended in
1289 resuspension buffer [(5 mM HEPES, pH 7.5, KOH), 10 mM EDTA (pH 7.5, NaOH), 1x protease inhibitor
1290 "complete EDTA-free" (Roche)]. For the disruption of cells, bead-beating was performed using a mini
1291 beadbeater (Biospec) in two cycles of 30 sec min^{-1}, with a 1 min period of cooling on ice between cycles.
1292 Disrupted cells were centrifuged at 4°C, 30 min, 14000 x g in a microfuge. The supernatant was removed,
1293 the pellet was resuspended in sample buffer (resuspension buffer supplemented with 100 mM Na_2CO_3, 100
1294 mM DTT, 2% WT/vol SDS, and 12% WT /vol sucrose).

1295 SDS-PAGE was performed using a 12% polyacrylamide gel (Bio-Rad), with the electrophoresis for 90 min
1296 at 120 V. Next, proteins were transferred onto a PVDF membrane (Bio-Rad) using Trans-Blot Turbo (Bio-
1297 Rad). The detection was performed using Clarity Max Western ECL Substrate (Bio-Rad).

1298

1299 **RT-qPCR**

1300 RT-qPCR, was performed as described previously(Kaye et al., 2019). Briefly, total RNA was isolated using
1301 the RNeasy Plant Mini Kit (Qiagen) and treated with DNase I (Qiagen). First-strand cDNA was generated
1302 by reverse transcription of 0.5 µg total RNA using the iScript cDNA Synthesis Kit (Bio-Rad). Real-time
1303 PCR using the Roche Light Cycler 480 was performed with the SensiMix NO-Rox SYBR Green I Kit as
1304 described by the manufacturer (Bioline). Oligos used in this research for analyzing the expression levels of
1305 Cre*TPT10/PPT2/TPT3/CGL51* are listed in **Supplemental Table 1**.

1306 **Analysis of transcript levels in response to different conditions**

1307 In order to analyze the transcript level of Cre*TPT* genes under different conditions, we obtained RNAseq
1308 data published previously in which cells experienced a diurnal cycle, nitrogen starvation, sulfur starvation
1309 and Fe^{2+} starvation(González-Ballester et al., 2010; Ngan et al., 2015; Strenkert et al., 2019; Urzica et al.,
1310 2013; Zones et al., 2015). The log2 fold change of each gene was calculated based on the ratio of transcript
1311 abundance at different time point over transcript level at time point 0 h. The fold change was visualized by
1312 a heatmap and the color bar is the scale of log2 (fold-change).

1313 **In vivo polymeric carbohydrate staining**

1314 Lugol's iodine (aqueous solution of 1.8% iodine and 3.0% potassium iodide) was used to stain in vivo
1315 polymeric carbohydrate. Briefly, 0.5 mL of the cell culture was pelleted, resuspended in 10 µL of Lugol's
1316 iodine and visualized under a bright-field microscope. Lugol's iodine selectively binds to alpha-1,4 glucans
1317 and stains it blue-black.

oligo name	sequence
gTPT3_pRam118_f	tactcacaacaagcccagttATGGCTTCGCTCGCTCAGCGCGTGAGC
gTPT3_pRam118_r	agcggggatccttatccgttTTAGGCCGCGGCCGGCGACGC
TPT3pro1000_f	gccttttgctcacatgtggcggccgccgccatgctggccaacag
TPT3pro1000_r	taccaatccacaaatgtgggctagcccatgtgaaggcgttgacc
TPT3_3UTR_f	gatgacgacaagtaaagatctTAAGGCGGGCAGCGGC
TPT3_3UTR_r	GCGCAAGAAAGAAGCTTGATATCCCCCTTATAATGTTTACAAGTGGTGCG
hygro_crispr_f2	GGAACTGGCGCAGTTCCTCTG
hygro_crispr_re2	GGCTCGCGTAGGAATCATCCG
TPT3_gRNA1_F	GCTCGGTTGAGCGCACCC
TPT3_gRNA1_R	CAAGGGTCTGGCGAGCACG
TPT3_gRNA2_F	ACCTCCCCATCGCCACGAT
TPT3_gRNA2_R	AGGGGTAAGGACAGCGGTG
Qrt_TPT10_f2	CCTGTACCAGCAGGTGTCGTAC
Qrt_TPT10_r2	CCAGCGCGTTCTGGAGTGACA
Qrt_PPT2_f2	ATGGCGTCTCTGCTGGGC
Qrt_PPT2_r2	CTGCTCGCCCATTCTCCTC
Qrt_TPT3_f2	GCAAAGCTGGCGCCTACTG
Qrt_TPT3_r2	TAGACCAGGCCGACCACCAC
Qrt_CGL51_f1	CTGGTTCATCGGGACATGGC
Qrt_CGL51_r1	TGGCTGAAGCTGACCACT

Supplementary Table 1: Oligonucleotide list.

ID	Construct	Restriction enzyme for transformation	Localization
pMBS472	PSADpro::aadA::PSAD-T:::: ARpro::roGFP2-Tsa2ΔCR::MStop::RPL23-T	ECoRV/AfeI	cytosol
pMBS652	PSADpro::aadA::PSAD-T:::: ARpro::CDJ1::roGFP2-Tsa2ΔCR::MStop::RPL23-T	ECoRV/AfeI	stroma
pMBS657	PSADpro::aadA::PSAD-T:::: ARpro::roGFP2-Tsa2ΔCR::SV40::RPL23-T	ECoRV/AfeI	nucleus
pMBS655	PSADpro::aadA::PSAD-T:::: ARpro::HSP70C::roGFP2-Tsa2ΔCR::MStop::RPL2	ECoRV	mitochondrion

Supplementary Table 2: Plasmids of H_2O_2 roGFP2-Tsa2ΔCR sensors (Niemeyer et al., 2021)**.**

Cre ID	Name from V6.1 / (name used in this study)	Previous name	Prediction	CS Position
Cre08.g379350_4532	**TPT10 / (TPT10)**	**TPT1**	**cTP**	**CS pos: 61-62. TCL-AV. Pr: 0.3994**
Cre06.g263850_4532	**N / (PPT2)**	**PPT2; TPT2; TPT20**	**cTP**	**CS pos: 70-71. VCQ-AA. Pr: 0.5253**
Cre01.g045550_4532	**TPT3 / (TPT3)**	**TPT3**	**cTP**	**CS pos: 60-61. VTK-AS. Pr: 0.4178**
Cre02.g106200_4532	N	TPT4; TPT5	OTHER	
Cre02.g112900_4532	N	TPT5; TPT6	OTHER	
Cre02.g144300_4532	N	TPT6; TPT7	OTHER	
Cre03.g162000_4532	N	TPT7; TPT8	OTHER	
Cre03.g184850_4532	N	TPT8; TPT9	OTHER	
Cre04.g227450_4532	N	TPT9	OTHER	
Cre07.g330850_4532	N	TPT10; TPT11	OTHER	
Cre08.g363600_4532	N	TPT11; TPT12	OTHER	
Cre09.g408400_4532	N	TPT12; TPT13	OTHER	
Cre09.g413700_4532	N	TPT13; TPT14	OTHER	
Cre08.g382350_4532	EZY14	TPT14; TPT16; EZY14	OTHER	
Cre09.g415900_4532	MOT20	TPT15	OTHER	
Cre10.g452750_4532	N	TPT16; TPT18	OTHER	
Cre11.g479950_4532	CGL7	TPT17	OTHER	
Cre12.g490050_4532	N	TPT18; TPT19; GMT1	OTHER	
Cre12.g490100_4532	TPT2	TPT19;GMT2	OTHER	
Cre12.g501000_4532	N	TPT20; TPT22; PPT1	OTHER	
Cre15.g641266_4532	N	TPT22; TPT23	OTHER	
Cre15.g642950_4532	N	TPT23; TPT24	OTHER	
Cre15.g643385_4532	N	TPT24; TPT26	OTHER	
Cre16.g663800_4532	**CGL51 / (CGL51)**	**TPT25**	**cTP**	**CS pos: 70-71. IVA-SS. Pr: 0.4817**
Cre16.g666250_4532	N	TPT26; TPT27	OTHER	
Cre17.g702700_4532	N	TPT27; TPT28	OTHER	
Cre17.g703250_4532	SLC35D	TPT28; TPT29	OTHER	
Cre17.g710850_4532	N	TPT29; TPT4	OTHER	
Cre11.g467754_4532	N	UAA6	OTHER	
Cre14.g622700_4532	N	N	OTHER	
Cre18.g748947_4532	N	N	OTHER	
Cre09.g408428_4532	N	N	OTHER	

Supplementary Table 3: Members of the triose phosphate transporter family in *Chlamydomonas reinhardtii* and their predicted subcellular localization based on TargetP-2.0. cTP, chloroplast transit peptide; CS position, transit peptides cleavage site; N: genes without names in the genome. Cre IDs are from v6.1 genome.

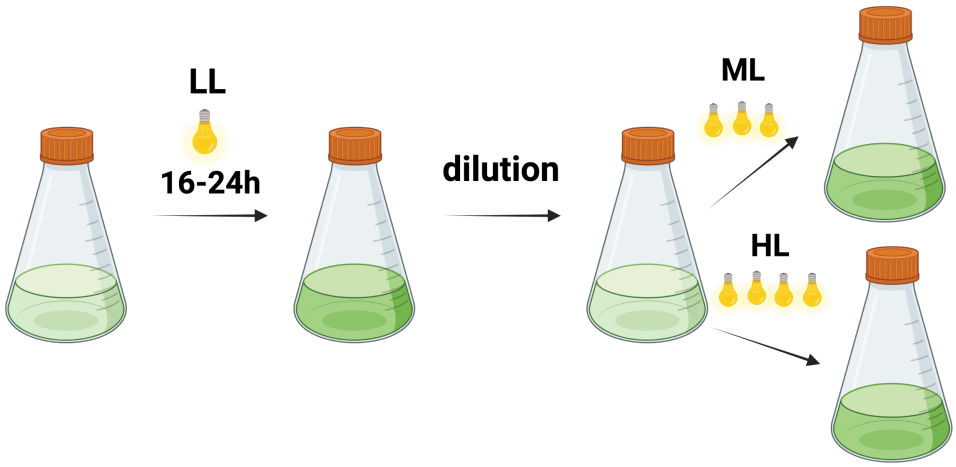

1329

1330 **Supplementary Fig. 1: Experimental set up.** All strains were grown photoautotrophically under low
1331 white light (LL, 30 µmol photons m^{-2} s^{-1}) for 16-24 h. After dilution with fresh medium, the cultures were
1332 transferred to moderate light (ML, 250-300 µmol photon m^{-2} s^{-1}) for 24 or 48 h. On occasion, the cultures
1333 were also transferred to the high light (~450 µmol photon m^{-2} s^{-1}). To avoid self-shading, the culture density
1334 was adjusted to 1-1.5 µg/mL chlorophyll before exposure to ML or HL.

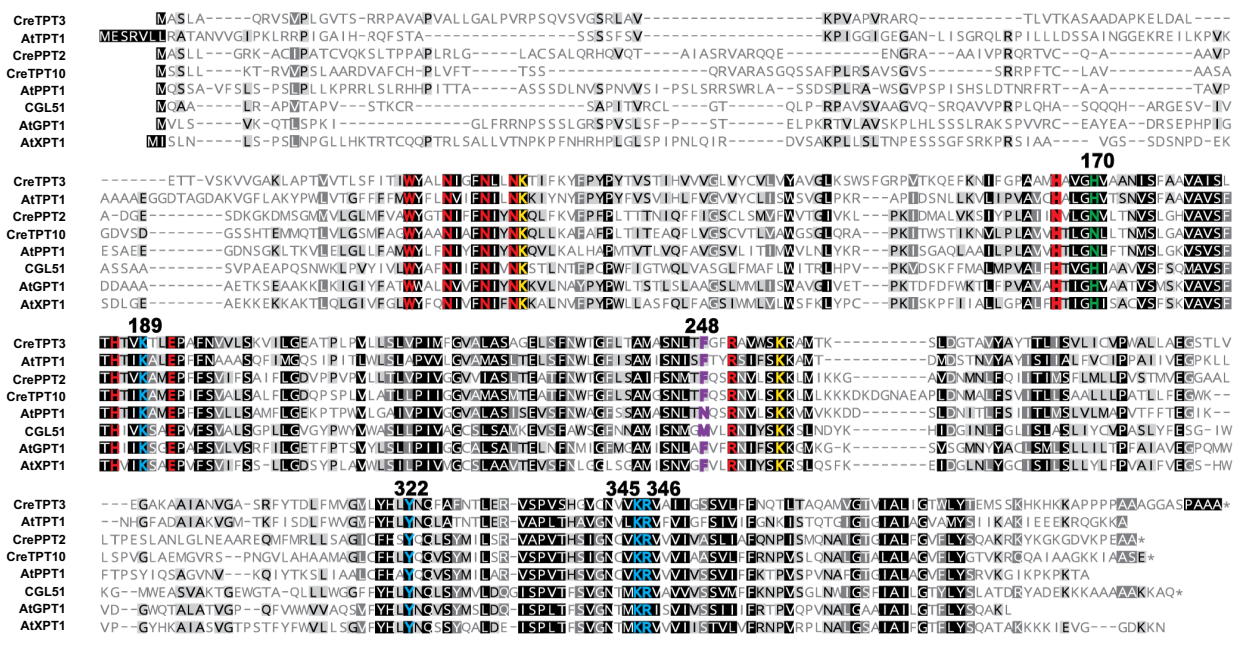

Supplementary Fig. 2: Alignment of putative plastid phosphate transporter sequences of *Arabidopsis thaliana* and *Chlamydomonas reinhardtii.* Plastid putative sugar phosphate transporters from Chlamydomonas are CreTPT10 (Cre08.g379350_4532), CrePPT2 (Cre06.g263850_4532), CreTPT3 (Cre01.g045550_4532), and CGL51 (Cre16.g663800_4532). Sequences from *Arabidopsis thaliana* are AtTPT1 (AT5G46110.1), AtPPT1 (AT5G33320.1), AtGPT1 (AT5G54800.1) and AtXPT1 (AT5G17630.1). Conserved substrate binding pockets are colored red. Phosphate-binding residues are colored blue. The gate capping residues are colored yellow. The positions of residue in green are crucial for the preference of triose-phosphate or 3-PGA as substrate. The purple residues are critical for the specificity of PEP.

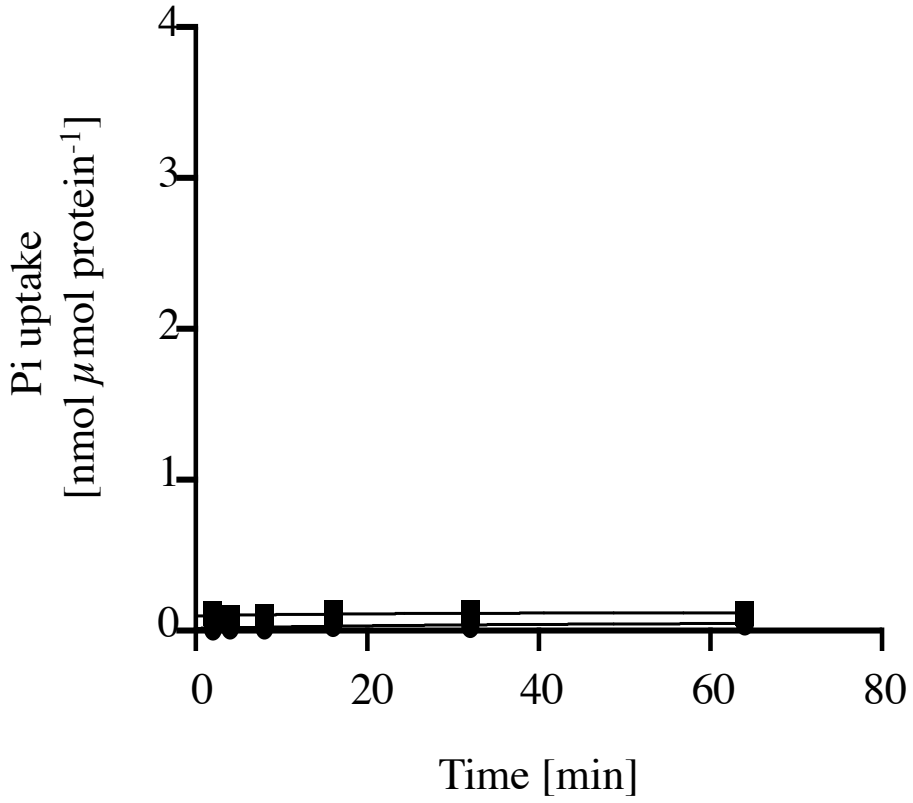

1347

1348 **Supplementary Fig. 3: Background activity of Pi uptake derived from the endogenous yeast**
1349 **transporters reconstituted into liposomes.** Time-dependent uptake of Pi (0.25 mM) into reconstituted
1350 liposomes preloaded with 30 mM of Pi (■) or without exchange substrate (●) prepared from yeast cells
1351 harboring the empty vector (pYES-NTa). The arithmetic mean (±SD) of three independent experiments
1352 (each with three technical replicates) was plotted against time. The observed Pi uptake rates of endogenous
1353 yeast carriers reconstituted into liposomes were negligible compared to the rates of His-CreTPT3 (20-fold
1354 higher, **Fig. 1C**), indicating that this expression system is suitable for functional analysis of recombinant
1355 phosphate transporters.

1356

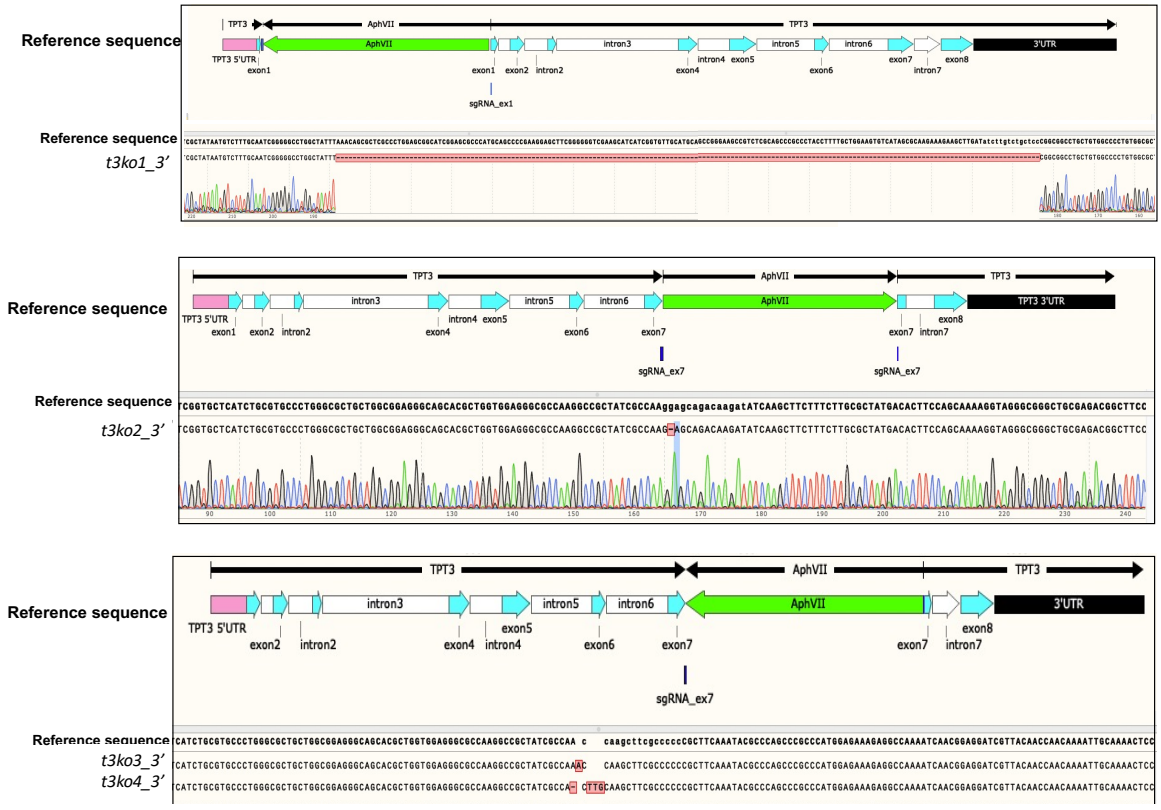

Supplementary Fig. 4: Sequencing of genomic DNA fragments across the site of insertion of the drug resistant marker (*AphVII* cassette, which confers hygromycin resistance) in the different *tpt3* mutants (*t3ko1*, *t3ko2*, *t3ko3* and *t3ko4*). The mismatched nucleotides are marked in pink.

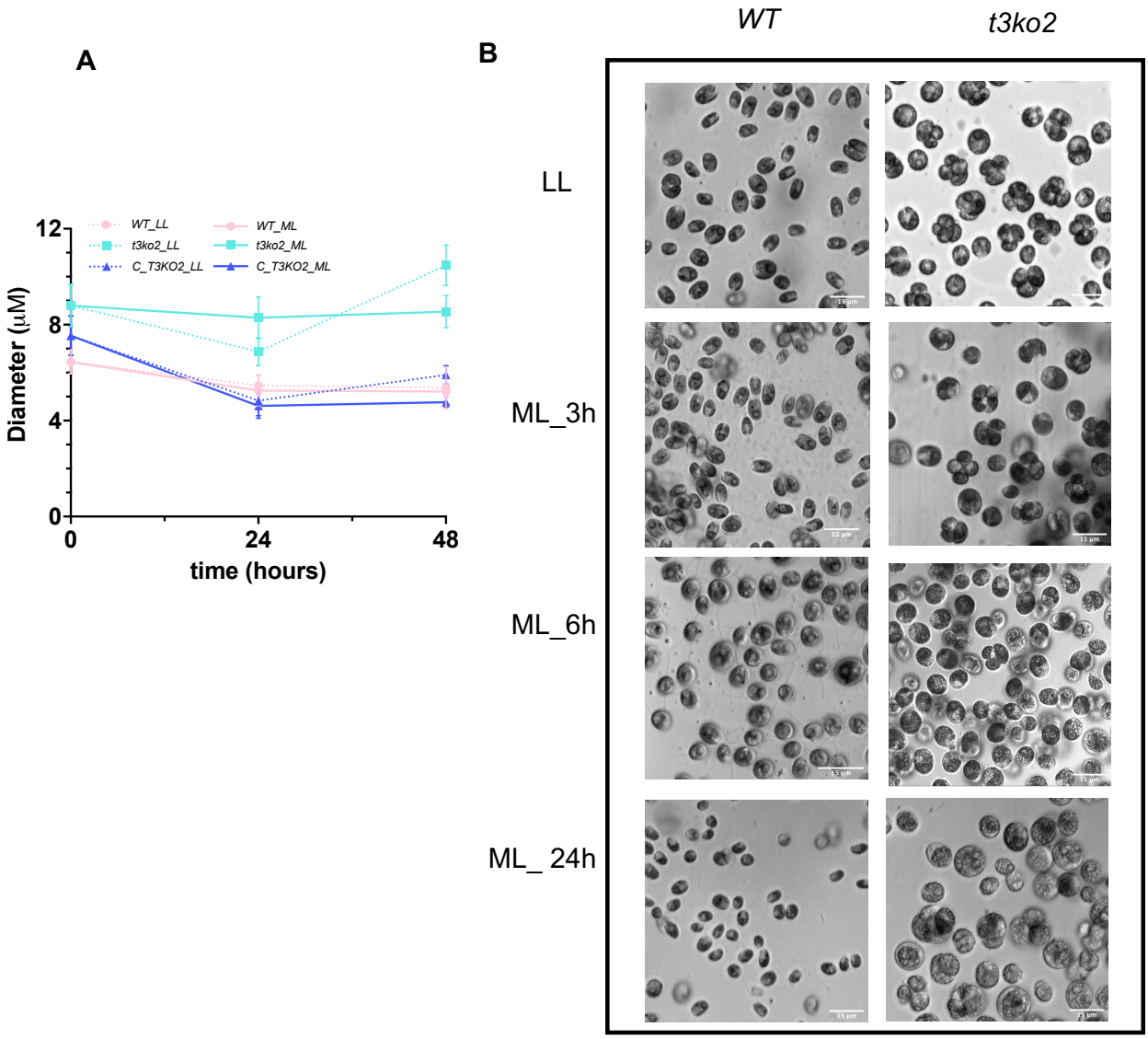

1362

1363 **Supplementary Fig. 5:** (**A**) Cell size of WT, *t3ko2*, and *C_T3KO2* in TP in both LL and ML. (**B**) WT and
1364 *t3ko2* morphology 24 h following a LL to ML transition.

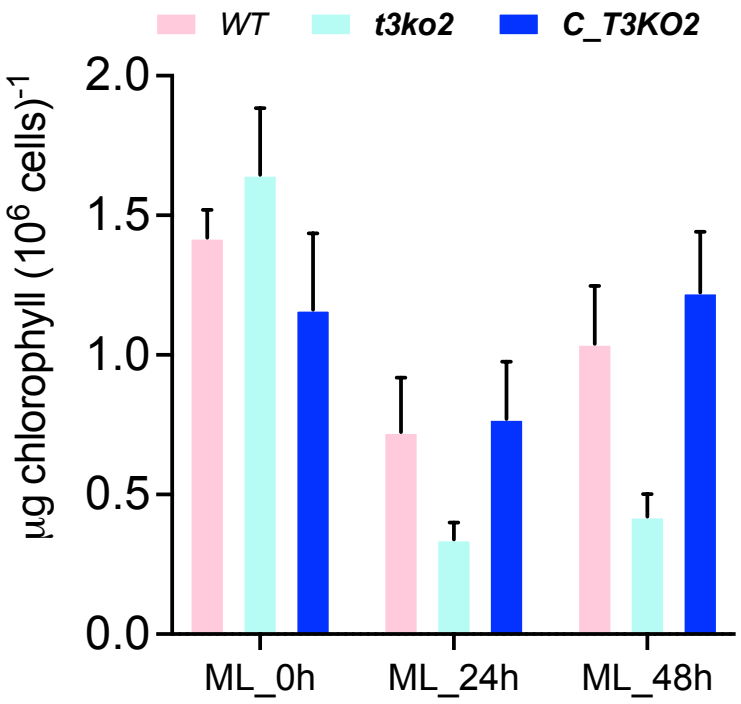

1365

1366 **Supplementary Fig. 6: Quantification of chlorophyll contents in indicated strains after exposure to**
1367 **ML for 24 and 48 h.** All strains were grown photoautotrophically in LL for 16-24 h. After dilution with
1368 fresh medium, the culture was transferred to ML and the chlorophyll content determined after 24 and 48 h
1369 in the ML. The initial inoculum density used for the transition was between 1-1.5 µg/mL chlorophyll in
1370 order to avoid self-shading.

1371

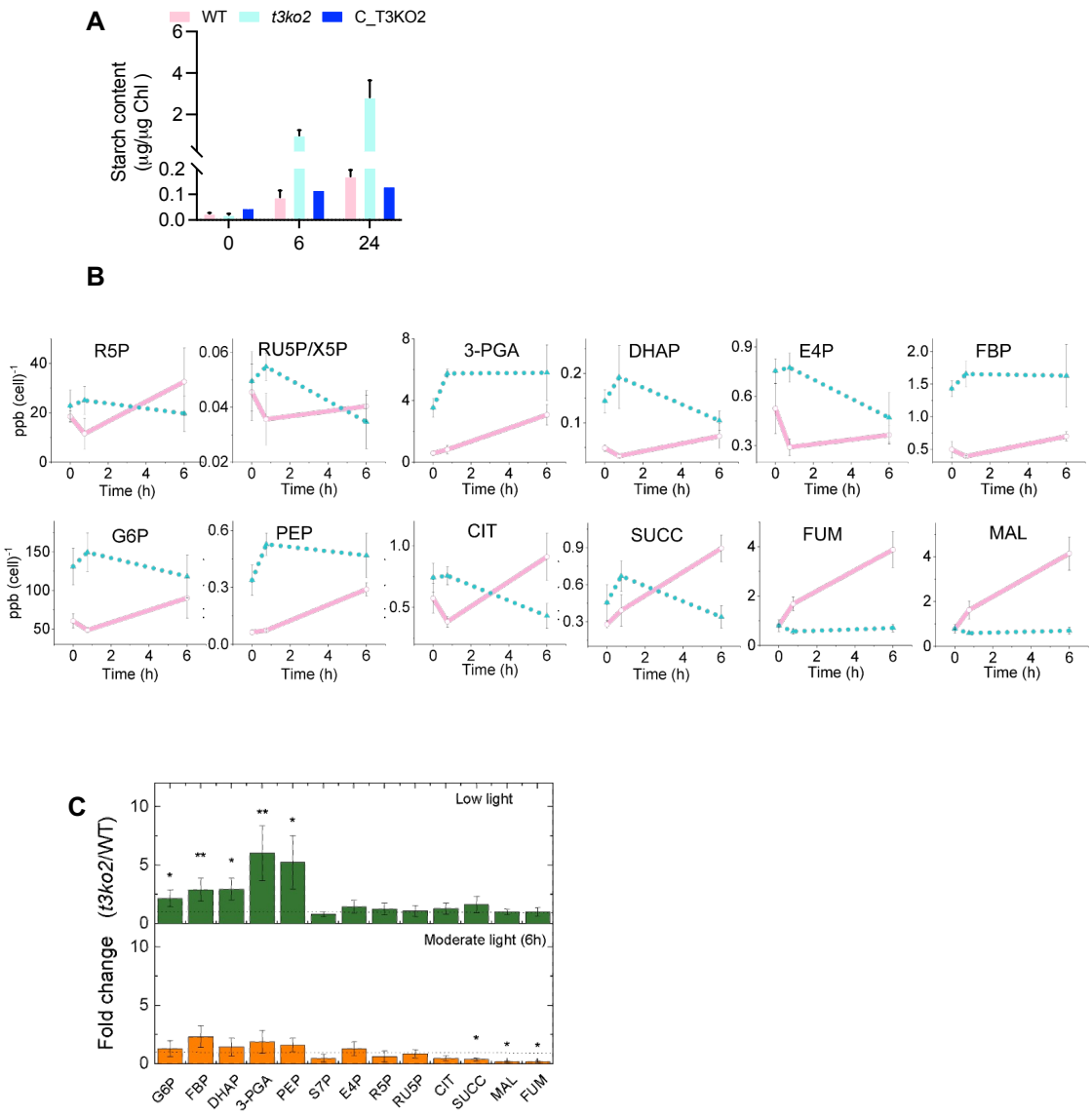

Supplementary Fig. 7: Starch and metabolites in WT and *t3ko2*. (**A**) Starch content in indicated strains following 0, 6, and 24 h in LL. (**B**) Time course, over a period of 6 sec, of change in metabolite pool sizes at 0 h (LL), 45 min and 6 h after shifting LL-grown cells to ML. Data was normalized to cell numbers. (**C**) Schematic representation of the fold-change for the metabolites shown in (**B**), calculated by dividing the pool size in *t3ko2* by that of WT cells under the same conditions. Fold change of 1 (no change) is shown by a dashed line. Each data point is the mean and standard error of three biological replicates. Asterisk indicates statistically significant differences relative to WT (* P<0.05, ** P<0.01, *** P<0.001). Abbreviations: G6P, glucose-6-phosphate; FBP, fructose bisphosphate; DHAP, dihydroxyacetone phosphate; 3-PGA, 3-phosphoglycerate; PEP, phosphoenolpyruvate; CIT, citrate; SUCC, succinate; FUM, fumarate; MAL, malate; S7P, sedoheptulose-7-phosphate; E4P, Erythrose 4-phosphate; R5P, Ribose 5-phosphate; RU5P/X5P, ribulose 5-phosphate/xylulose-5-phosphate.

1385

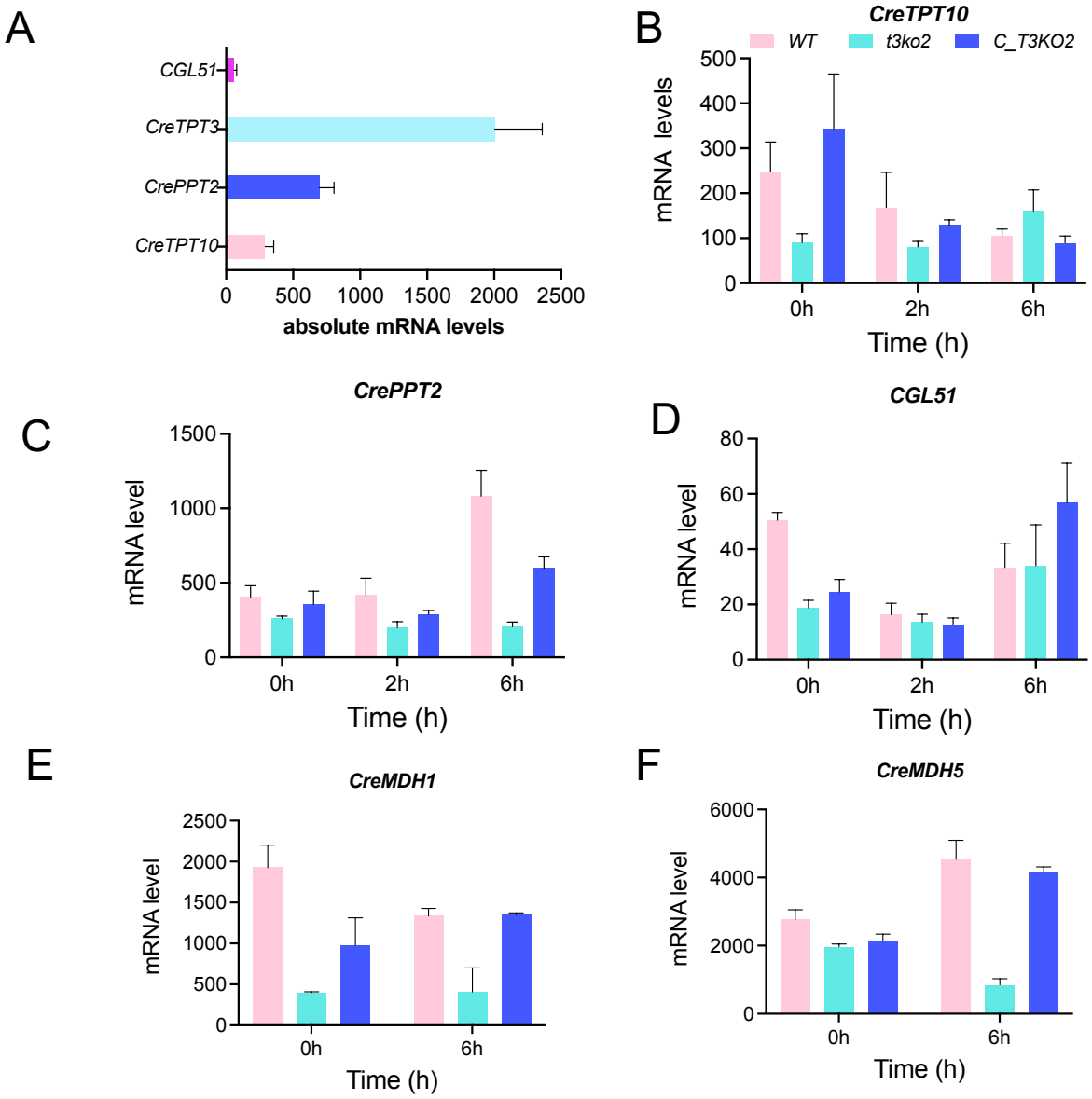

1386

1387 **Supplementary Fig. 8:** (**A**) mRNA levels encoding putative chloroplast envelope localized TPTs under
1388 LL during growth in TP medium. mRNA levels of CreTPT10 (**B**), CrePPT2 (**C**) and CGL51 (**D**) in the
1389 indicated strains 0, 2, 6 h after the cells were shifted from LL to ML. (**E, F**) mRNA levels of plastidial
1390 malate dehydrogenases (MDH) in the indicated strains 0, 6 h after the cells were shifted from LL to ML.

1391

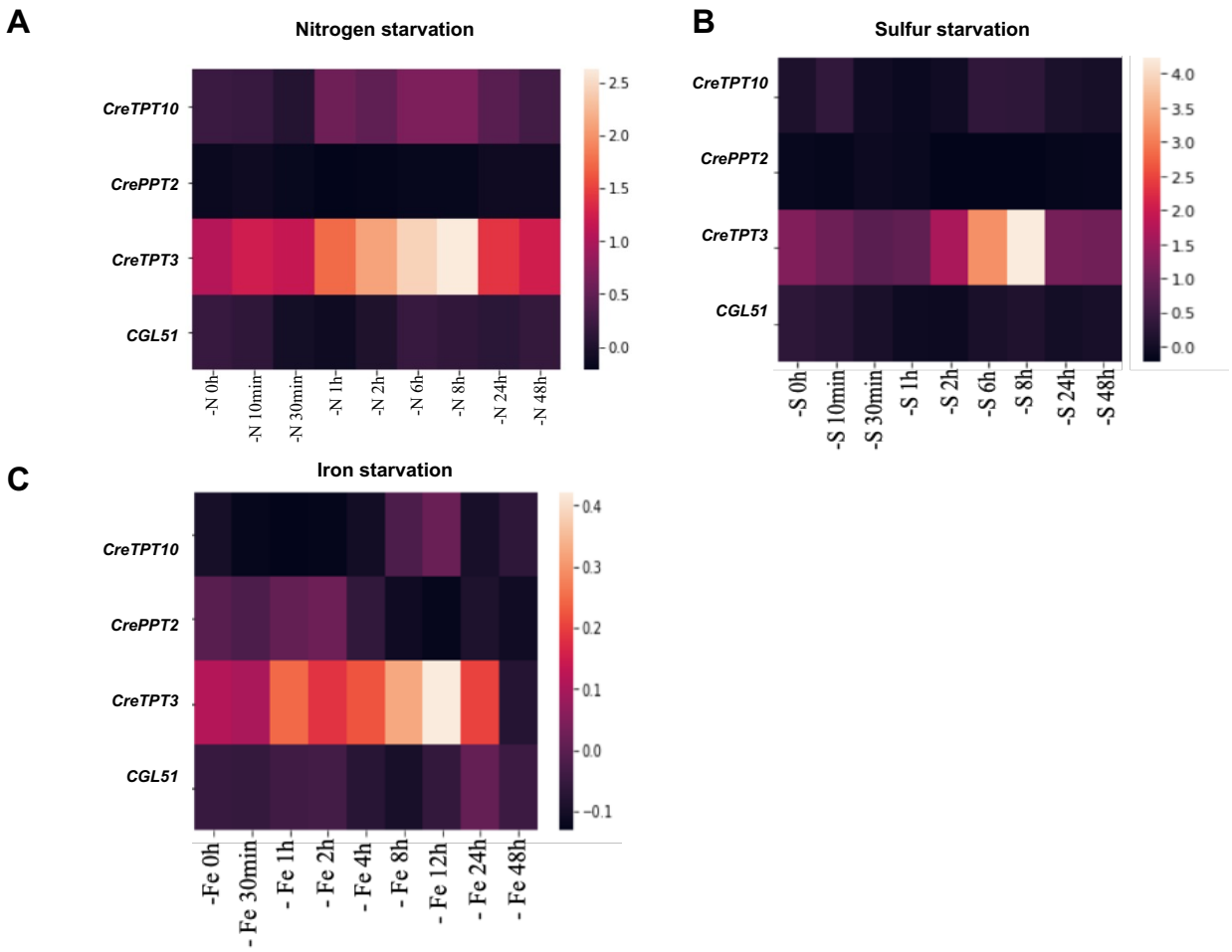

Supplementary Fig. 9: Expression of the putative chloroplast envelope localized TPTs under nitrogen starvation **(A)**, sulfur starvation **(B)**, and iron starvation **(C)** (González-Ballester et al., 2010; Ngan et al., 2015; Urzica et al., 2013).